SOLIDIFICATION AND MICROSTRUCTURE FORMATION OF NICKEL BASED SUPERALLOY 718PLUS

A THESIS SUBMITTED TO
THE GRADUATE SCHOOL OF NATURAL AND APPLIED SCIENCES
OF
MIDDLE EAST TECHNICAL UNIVERSITY

BY

BERKHAN KARADEDE

IN PARTIAL FULFILLMENT OF THE REQUIREMENTS
FOR
THE DEGREE OF MASTER OF SCIENCE
IN
METALLURGICAL AND MATERIALS ENGINEERING

JANUARY 2025

Approval of the thesis:

SOLIDIFICATION AND MICROSTRUCTURE FORMATION OF NICKEL BASED SUPERALLOY 718PLUS

submitted by **BERKHAN KARADEDE** in partial fulfillment of the requirements for the degree of **Master of Science** i**n Metallurgical and Materials Engineering, Middle East Technical University** by,

Prof. Dr. Naci Emre Altun
Dean, **Graduate School of Natural and Applied Sciences** _____

Prof. Dr. Ali Kalkanlı
Head of the Department, **Metallurgical and Materials Eng.** _____

Prof. Dr. Ali Kalkanlı
Supervisor, **Metallurgical and Materials Eng., METU** _____

Examining Committee Members:

Prof. Dr. Y. Eren Kalay
Metallurgical and Materials Eng., METU _____

Prof. Dr. Ali Kalkanlı
Metallurgical and Materials Eng., METU _____

Prof. Dr. M. Vedat Akdeniz
Metallurgical and Materials Eng., METU _____

Assist. Prof. Dr. Şeniz Uçar
Metallurgical and Materials Eng., METU _____

Prof. Dr. Abbas Tamer Özdemir
Metallurgical and Materials Eng., Gazi University _____

Date: 09.01.2025

I hereby declare that all information in this document has been obtained and presented in accordance with academic rules and ethical conduct. I also declare that, as required by these rules and conduct, I have fully cited and referenced all material and results that are not original to this work.

Name Last name : Berkhan Karadede

Signature :

ABSTRACT

SOLIDIFICATION AND MICROSTRUCTURE FORMATION OF NICKEL BASED SUPERALLOY 718PLUS

Karadede, Berkhan
Master of Science, Metallurgical and Materials Engineering
Supervisor: Prof. Dr. Ali Kalkanlı

January 2025, 81 pages

Alloy 718Plus™ is a Ni-based superalloy developed by ATI Allvac to increase Alloy 718 maximum service temperature by 55°C. Alloy 718 is widely used in aero gas turbine engines for its excellent performance at temperatures up to 649 °C. Alloy 718 stands out due to its favorable qualities, such as good forgeability, castability, and weldability. With advancements in gas turbine engine technology increasing the overall temperature capacity, the demand for cast static parts operable at higher temperatures is also evolving. Alloys like Rene 41 and Waspaloy can withstand higher temperatures than 649 °C; however, they present challenges in shaping, welding, and manufacturing. The Alloy 718 to 718Plus™ modification has made it a great alternative for applications requiring performance between 649°C and 760°C. 718Plus has already been used in forged form for gas turbine engines in the industry. This thesis explores the potential application of this alloy in cast form for static components. The effects of two different mould types—sand and metal—on the microstructure are compared. Alloy 718Plus™ was produced through induction melting under a protective argon atmosphere. Both revert 718 alloy and elemental raw materials were used in alloying 718Plus™. Metal moulds produced finer dendritic structures. Homogenization of both castings showed different results. In

sand casting, Laves phase dissolution is successfully achieved. However, in castings from metal moulds, Laves phases were not fully dissolved even after homogenization, showing brittle behavior. After solution treatment and aging, laves phase along the grain boundary were increased.

Keywords: Nickel-base superalloy, Alloy 718Plus^{TM}, Laves phase, Sand mould

ÖZ

NİKEL BAZLI 718PLUS SÜPERALAŞIM KATILAŞMA DAVRANIŞI VE MİKROYAPI OLUŞUMU

Karadede, Berkhan
Yüksek Lisans, Metalurji ve Malzeme Mühendisliği
Tez Yöneticisi: Prof. Dr. Ali Kalkanlı

Ocak 2025, 81 sayfa

718Plus™ Nikel bazlı süper alaşımı, ATI Allvac tarafından 718 alaşımının maksimum servis sıcaklığını 55°C artırmak için geliştirilmiştir. 718 alaşımı, 649 °C'ye kadar olan sıcaklıklarda mükemmel performansı nedeniyle aero gaz türbini motorlarında yaygın olarak kullanılır. Aynı zamanda 718 nikel alaşımı, iyi dövülebilirlik, dökülebilirlik ve kaynaklanabilirlik gibi olumlu nitelikleri nedeniyle de öne çıkmaktadır. Gaz türbini motorlarda türbin parçaları çalışma sıcaklıkları artırdıkça, daha yüksek sıcaklıklarda çalışabilen döküm parçalara olan talep de artmaktadır. Rene 41 ve Waspaloy gibi alaşımlar 649 °C'nin üzerinde sıcaklıklara dayanabilir; ancak şekillendirme, kaynaklama ve üretim süreçlerinde zorluklar ortaya çıkarmaktadır. 718 Alaşımı'nın 718Plus'a dönüştürülmesi, onu 649 °C ile 760 °C arasında performans gerektiren uygulamalar için mükemmel bir alternatif haline getirmiştir. 718Plus, gaz türbin motorlarında dövme formunda kullanılmaktadır. Bu tez, bu alaşımın döküm formunda statik bileşenler için potansiyel kullanımını araştırmayı amaçlamaktadır. İki farklı kalıp tipinin (kum kalıp ve metal kalıp) mikro yapı üzerindeki etkileri karşılaştırılmıştır. 718Plus alaşımı, koruyucu argon atmosferi altında indüksiyon ergitme yöntemiyle üretilmiştir. Alaşımlama sürecinde hem hurda 718 Alaşımı hem de saf hammaddeler kullanılmıştır. Metal kalıplar, daha

ince dendritik yapılar üretmiştir. Her iki dökümün homojenizasyon ısıl işlemi sonucunda farklı davranış göstermiştir. Kum dökümde, Laves fazının çözünmesi başarıyla sağlanmıştır. Ancak metal kalıptan üretilen dökümlerde, homojenizasyon işlemine rağmen Laves fazları tamamen çözünmemiş ve kırılgan bir davranış sergilemiştir. Aynı dökümde çözeltiye alma ve yaşlandırma sonrasında tane sınırlarında lave fazları gözlemlenmiştir.

Anahtar Kelimeler: Nikel bazlı süperalaşımlar, 718Plus™ alaşımı, Kum Kalıp, Lave fazları

To My Grandparents,

Neriman & Salih

ACKNOWLEDGMENTS

I would like to extend my heartfelt thanks to my supervisor, Prof. Dr. Ali Kalkanlı, for providing me with the invaluable opportunity to pursue my studies in an industry I am deeply passionate about. I am truly grateful for his mentorship, endless support, and encouragement throughout this research.

I am also sincerely thankful to Salih Türe for his selfless assistance in my casting processes and throughout the experimental studies. My deepest appreciation goes to Ramazan Karataş for his dedication to all the laboratory work and for enduring my keen attention to detail. I am also grateful to Cengiz Mehmet Tan for his support with the SEM analysis and to Cemal Yanardağ and Önder Şahin for their contributions to the mechanical testing.

I am incredibly thankful to my colleagues, Hanifi Eray Korkmaz and Sergen Halim Ayhan, for their constant support through every challenge at work. Their trust in me has been a driving force, helping me push forward and gain invaluable experience. Their patience and advice, especially during my most challenging moments, have truly meant the world to me.

Special thanks to my family, my most cherished supporters, whose encouragement and belief in me have been a constant source of strength and inspiration throughout the struggles I have faced in life. Finally, Thank you, my love, Sıla, for always being there for me with your endless kindness and cheerfulness.

TABLE OF CONTENTS

LIST OF TABLES

TABLES

LIST OF FIGURES

FIGURES

LIST OF ABBREVIATIONS

ABBREVIATIONS

AMS	Aerospace Material Specification
BCT	Body Centered Tetragonal
BSE	Backscattered Electrons
CALPHAD	Calculation of Phase Diagrams
CCT	Continous Cooling Transformation
Co-based	Cobalt-Based
EDS	Energy Dispersive Spectroscopy
ESR	Electro-Slag Remelting
FCC	Face Centered Cubic
HCP	Hexagonal Close Packed
SEM	Scanning Electron Microscope
MC	Metal Mould Castings
Ni-based	Nickel-Based
PM	Powder Metallurgy
SC	Sand Castings
TCP	Topological Close Packed
TEM	Transmission Electron Microscopy
TTT	Time-Temperature-Transformation
VAR	Vacuum Arc Remelting

VIM	Vacuum Induction Melting
SDAS	Secondary Dendrite Arms Spacing

LIST OF SYMBOLS

SYMBOLS

T_L	Liquidus Temperature
T_S	Solidus Temperature
Γ	Gibbs Thomson Coefficient
λ_{SD}	Secondary Dendritic Arm Spacing
γ	Austenitic FCC Ni-matrix
γ'	$Ni_3(Al,Ti)$ phase
γ''	Metastable Ni_3Nb phase
σ	Sigma Phase
μ	Mu Phase
%	Percentage
at%	Atomic Percentage
wt%	Weight Percentage

CHAPTER 1

INTRODUCTION

1.1 Background

Nickel Base Superalloys play a critical role in aero turbine gas engines, continually evolving to improve efficiency through increased operating temperature and the component lifetime under conditions of high temperatures, stresses, and corrosive environments. Nickel-based Superalloys can be categorized in various ways, including by microstructure, application, and production method. Based on microstructure, these alloys are typically classified into two groups: solid solution strengthened and precipitate-strengthened systems. Precipitate-strengthened alloys are often divided into three sub-categories: γ' (gamma-prime) and γ″ (gamma-double-prime). Solid solution-strengthened alloys are advantageous for applications requiring extremely high temperatures, such as combustion chambers and exhaust liners, due to the lack of concern for the dissolution of precipitate phases. On the other hand, precipitation-strengthened alloys operate in environments with high-stress levels at lower temperatures. These alloys are designed to exhibit excellent fatigue and creep resistance required in rotating parts of an aero-turbine gas engine.

Inconel 718 γ″ precipitates strengthened alloy widely used in the aerospace industry due to its excellent formability, weldability, machinability, and outstanding mechanical properties. However, its maximum service temperature is limited to 649 °C. Above 649°C, γ″ precipitates begin to coarsen rapidly and transform into the stable phase δ, which, in excessive amounts, is detrimental to mechanical properties, potentially causing catastrophic failure[1]. Operating temperatures should be higher for better efficiency in the gas turbine engine industry. Due to the limitations of Inconel 718, γ′ alloys like Rene 41 and Waspaloy are used for higher temperatures. Unlike alloy 718, γ′ strengthened alloys are challenging to weld and machine,

significantly increasing manufacturing costs and complicating process development[2]. GE Aerospace, Pratt-whitney, Allvac, Carpenter Technology, and Honeywell like large companies and manufacturers in the aerospace industry proposed a Metal Affordability Initiative (MAI) program in the early 2000s funded by the US Airforce to develop low-cost structural material that can operate at high temperatures[3]. 718Plus™ is one of the proposed alloys by Allvac with a 55°C more maximum service temperature to fill the gap between Alloy 718 and Waspaloy-like gamma prime alloys which both alloys recommended maximum service temperatures are 649°C and 760°C[1,4]. 718Plus™ is a trademark of Allvac, ATI - Allegheny Technologies Incorporated[1]. Throughout this thesis, it will be referred to as 718Plus for simplicity.

1.1.1 Gas Turbine Engines

Gas Turbine Engines are heat engines that draw air and are used for thrusts. Gas turbine engines are widely used across aviation, energy, and marine industries, each with different working conditions and requirements. However, all works with similar principles.

A gas turbine engine operates through four main stages: air inlet, compression, combustion, and exhaust. The air inlet directs atmospheric air smoothly into the engine, where it then enters the compression stage. Here, rotating and stationary blades compress the air, increasing its pressure and temperature to create a dense, high-energy flow. This compressed air mixes with fuel and ignites in the combustion chamber, releasing significant heat energy and raising the airflow temperature [5]. The resulting high-energy gases then pass through the exhaust stage, where a turbine is rotated using energy from the flow to drive the compressors, and the remaining gases exit as a fast-moving jet stream[5].

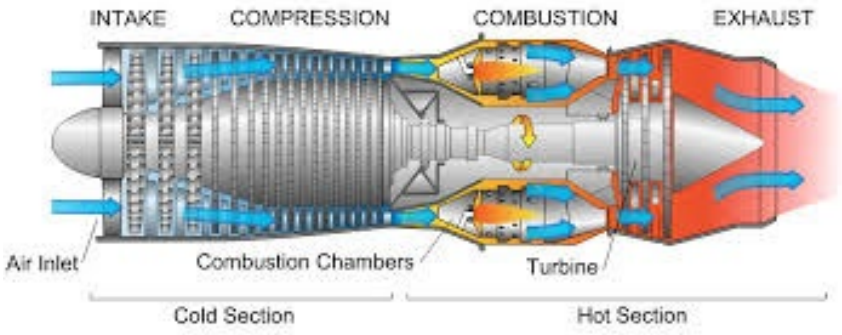

Figure 1.1 Gas Turbine Engine Section Schematics[5].

Each section has specific material usage depending on the operating temperatures and conditions. The air inlet remains cool and must resist corrosion, making aluminum and titanium alloys ideal materials due to their low weight and high strength properties. As temperature increases through the compressor section, titanium alloys are more common due to their strength at moderate temperatures. However, temperatures can become too high at the last compressor stages, making nickel-based superalloys a better option. The combustion chamber and nozzle operate at very high temperatures. Ni- and Co-based superalloys mainly form each component located in these sections. The highest temperatures are typically found in the combustion chamber, where solid solution-strengthened alloys such as Hastelloy X, Haynes 230, and 188 are used as inner walls. For the combustion case, In718-like alloys can be picked. The turbine section contains vanes, turbine disk, and turbine blade connected to the disk that powers the compressors. Since this section operates at high temperatures, failures like creep and thermomechanical fatigue critical. Alloys like Rene95, Rene88, Inconel 738, Mar M247, and single crystal alloys are designed explicitly against these type of failures. Hot corrosion is also an important criterion in the turbine section, especially in marine and industrial applications[6,7], where alloy selection becomes very critical. Cobalt base superalloys are suitable corrosion-resistant alloys and an option for static parts that are expected to operate for long durations.

1.2 Motivation

Throughout the improvements in the designs of gas turbine engines, many solutions were found for alloys in turbine disks and turbine blades that can operate at higher temperatures with new thermal-barrier-coating and cooling applications[8,8–15]. Consequently, these improvements also increase the overall temperature of the whole engine, resulting in a reassessment of the requirements of all components. Gas turbine engines are massive, complex machines with many static parts and challenging geometries. Most of these parts are designed to contain air flow, and produced by investment casting to cut machining costs at high-volume production. Therefore, with over 649 °C operating temperature, 718 Alloy parts may undergo necessary changes to alloys like waspaloy in which castability and weldability are a problem, possibly increasing complexity, scrap amounts, and overall costs. Therefore, this thesis explores options to replace cast 718 with 718Plus for higher service temperature.

CHAPTER 2

LITERATURE REVIEW

2.1 Nickel Base Superalloys

2.1.1 Precipitation Hardening

The strength of an age-hardening alloy depends on the interaction between moving dislocations and precipitates. The precipitates act as barriers, where dislocations must either cut through or bypass them with a looping mechanism[16]. Consequently, hardening can caused by three main mechanisms: Coherency strain hardening and Chemical hardening, where dislocations cut through the precipitates[16].

Small precipitates or particles are coherent and deformable, allowing dislocations to cut through them. In large precipitate, however, become incoherent, causing dislocations to bypass them[16]. For deformable precipitates, where dislocations move through the precipitates, the precipitates's intrinsic properties become significant, resulting in only a slight variation in alloy strength with particle size[16]. For non-deformable particles, where dislocations bypass them, alloy strength depends heavily on particle size and dispersion along matrix, with strength decreasing as precipitate size or the inter-distance between precipitate increases[16]. Figure 2.1 illustrates the size and strengthening effect in coherent and non-coherent particles[16].

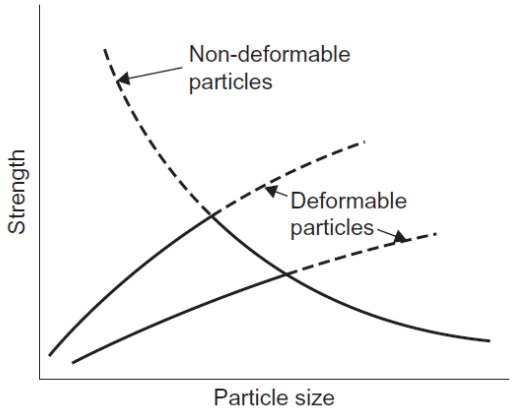

Figure 2.1. Strengthening mechanism relation with the precipitate size[16].

2.2 Superalloy Metallurgy

Nickel base superalloys consist of an austenitic fcc matrix phase, including various alloying elements for solid solution strengthening, such as chromium, iron, cobalt, tungsten, molybdenum, niobium, and more. Main strengthening precipitates that can be described as gamma-prime and gamma-double-prime which are denoted as γ′ and γ″, respectively. Secondary phases in the matrix are sometimes intentionally used to control the properties of alloys. The most common secondary phases can be named eta (η) hexagonal ordered Ni_3Ti, (δ) orthorhombic Ni_3Nb intermetallic compounds[17,18]. Several FCC carbides, such as MC, $M_{23}C_6$, M_6C, and M_7C_3, can potentially form in superalloys, though some may not be present in many alloy compositions[17,18]. Finally, detrimental phases have severe consequences for superalloys, especially after prolonged high-temperature exposure. Among these phases are σ, μ, and laves phases, which can also be named topologically close-phase (TCP) [17,18].

Classifying nickel alloys based on their strengthening mechanisms provides valuable insight into the applications of nickel-based superalloys. For instance, some of the most widely used solid solution-strengthened Ni-based superalloys include alloys 601, 617, 625, Hastelloy X, and Haynes 230. These alloys are commonly used in combustion chambers or exhaust components in the energy industry, where their

excellent corrosion resistance and high temperature properties are crucial. However, tensile strength is not the primary requirement in such applications. Meanwhile, precipitate-strengthened alloys are classified depending on primary strengthening phases, γ′, and γ″ as discussed earlier. Thermodynamically, γ′ is a stable precipitate and would dissolve at high temperatures, which makes γ′ alloys suitable to be used where high strength and creep resistance are required. Common alloys in this type are Waspaloy, Rene 41, Udimet 720, Astroloy, Rene 88DT, Inconel 738, MarM-247, and CMSX-4 (single crystal). Unlike γ′, γ″ precipitate is meta-stable and rapidly coarsens and dissolves or turns into delta phase at high temperatures. However, γ″ phase significantly enhances material strength at moderate temperatures, even in small quantities, as seen in alloys like Inconel 706 and Inconel 718. In particular, Inconel 718 is one of the most widely used superalloys, commonly found in components such as shafts, compressor disks, engine casings, and frames in gas turbine engines, and known to be weldable and easily machinable.

2.2.1 Elements Role

Common elements used as solid solution strengtheners in Ni-base superalloy are Co, Fe, Cr, Mo, W, Re, and Ru with the primary function of increasing strength and creep resistance[19]. The solubility of these elements can be evaluated by size factor. The solid solution-forming elements increase alloy strength by impeding dislocation movements by distortions and shear modulus shifts along the lattice. Due to alloying, stacking fault energy is lower, making dislocations cross slip difficult[19]. Improving creep resistance through solid solution strengthening relies on important factors such as low diffusivity, low stacking fault energy, and a high elastic modulus[19]. The diffusion coefficients decrease in the order of $D_{Cr,}$ $D_{Co,}$ $D_{Ta,}$ $D_{Mo,}$ $D_{Ru,}$ $D_{w,}$ and D_{Re}, with Rhenium having the lowest diffusion coefficient, making it an excellent alloying element, especially in single-crystal alloys used for turbine blades where creep is too significant[20]. The high melting solutes are the most preferred for creep resistance. Decreasing melting temperature is linked to lower

stacking fault energy, while the elastic modulus can either increase or decrease[20]. Tungsten and molybdenum have high melting points and strong hardening effects but suffer from low solubility in nickel[20].

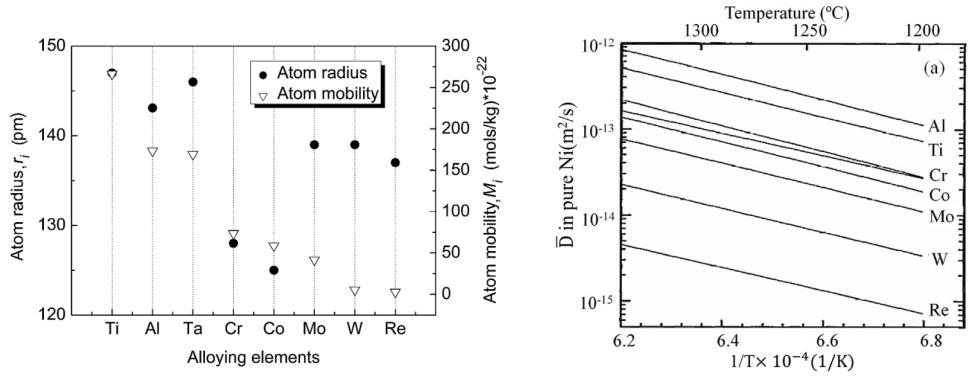

Figure 2.2. Atomic radius and mobility are given for specific elements and corresponding diffusivity in changing temperatures[21].

Aluminum, titanium, and niobium are precipitation-forming elements for γ′ and γ″ phases, as explained in the following sections. Cr, Nb, Ti, Mo, W, and Fe also form specific carbides, which are discussed in more detailed later. In summary, Table 2.1 lists roles of elements in Ni-base superalloys [17].

Table 2.1. Role of elements in Nickel Base Superalloys[17].

Features	Elements
Solid solution	Co, Cr, Fe, Mo, W, Ta, Re
Carbide formation:	
MC	W, Ta, Ti, Mo, Nb, Hf
M_7C_3	Cr
$M_{23}C_6$	Cr, Mo, W
M_6C	Mo, W, Nb
γ′ Ni_3(Al,Ti) former	Al, Ti
γ′ solvus temperature improvement	Co
Oxidation Resistance	Al, Cr, Y, La, Ce
Sulfidation Resistance	Cr, Co, Si
Improves Creep Properties	B, Ta
Grain Bondary Refiners	B, C, Zr, Hf
TCP Formation	Cr, Nb, W, Mo, Re, Co, Fe

2.2.2 Hardening Phases

2.2.2.1 γ′ (Gamma-Prime) Phase

The γ′ phase consists of an FCC crystal structure (L_{12}) with the chemical formula $Ni_3(Al, Ti)$, maintaining a high degree of coherency with the γ-matrix in between 0 – 0.5%. It can form spherical or cubic shapes depending on the alloying elements and temperature exposure[18,22]. The characteristic high coherency of γ′ reduces the coarsening rate, which is beneficial for turbine applications where temperature stability and creep resistance are significant. However, the nucleation rate is also very high for similar reasons, making the alloy challenging to form and weld[23]. Alloys with higher γ′ known for their resistance to creep and stresses at high temperatures[17,18,24,25]. γ′ value can reach 60 - 80%, where 65-70% is considered the optimum level for blade applications[11].

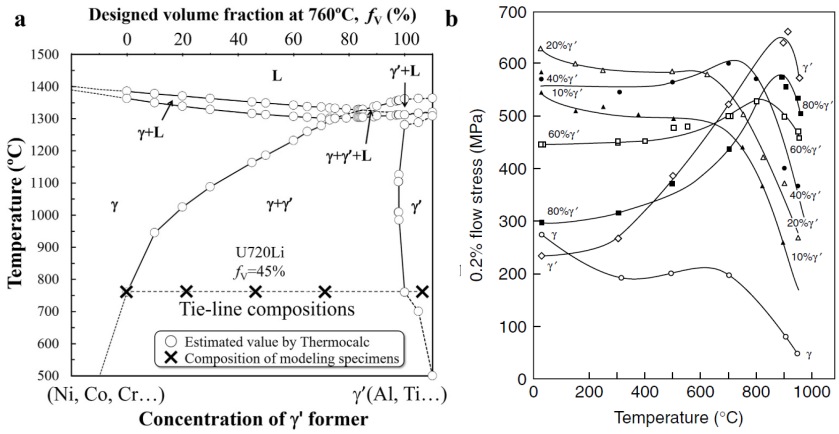

Figure 2.3. The variation in composition effect the precipitate amount and its impact on tensile properties across various temperatures[18,22].

2.2.2.2 γ″ (Gamma Double Prime) Phase

γ″ precipitates are metastable Ni_3Nb phase in the D022 body-centered tetragonal (BCT) structure and appear as coherent disc-shaped particles on the {100}

planes[26,27]. The lattice parameters are approximately c = 0.740 nm and a = 0.362 nm[17].

2.2.2.3 Nucleation of Precipitates

Even though the coarsening rate of the γ′ precipitate is slow, the rate of nucleation rate is relatively fast, especially when the amount of γ′ elements like aluminum, titanium, and tantalum is higher.

$$J = \frac{2CD}{a_o^4}\sqrt{\frac{\sigma}{k_B T}} \times e^{\left(-\frac{4\pi\sigma r^{*2}}{3k_B T}\right)} \times e^{(-\tau/t)} \tag{2.1}$$

The precipitation nucleation rate, represented by J, is determined by the above equation [28,29]. In this equation, D stands for solute diffusivity within the matrix, C denotes solute content in the matrix, α_0 represents the average lattice parameter of both the matrix and the precipitate, σ signifies surface energy, $k_B$is Boltzmann's constant, is Boltzmann's constant, T stands for temperature in kelvins, and t represents time. r^* designates the critical radius of precipitate to become a stable nucleus which is dependent to chemical free energy of the reaction ΔG^* and the elastic strain energy ΔG_p depending the coherency of the precipitate with the Ni-matrix[28,29].

$$r^* = \frac{2\sigma}{\Delta G^* + \Delta G_p} \tag{2.2}$$

The nucleation rate J is also related to the steady-state nucleation rate J_0 through the term $\exp(-\tau/t)$, which describes the initial nucleation transient where embryos with sub-critical radii are formed. The incubation time gets shorter when the critical radius is smaller and the equilibrium molar volume of precipitate increases[28,29]. High precipitation molar volume exhibits higher supersaturation,

which is the driving force of diffusion. Higher diffusivity also helps in favor of incubation time. However, high coherency reduces the rate of nuclei grow. Thus, coherency increases the incubation time. These relations can be easily observed with the equation below[28,29].

$$\tau = \frac{\pi R T r^{*3}}{96\, V_M D \sigma}$$

(2.3)

The precipitate's critical radius significantly influences the incubation time. To minimize the critical radius, it is essential to have low surface energy and higher bulk chemical energy, implying the need for greater undercooling[28,29].

2.2.2.4 Particle Coarsening

The microstructure of a two-phase alloy is always unstable, and interface-free energy should be minimum. Therefore, a high density of small precipitates will tend to coarsen into a lower density of large precipitates with smaller total interfacial areas. This is also known as Ostwald ripening.

In precipitation-hardened alloys, precipitates range in size due to variations in nucleation times and growth rates. The Gibbs-Thomson effect causes the solute concentration in the matrix near a particle to rise as the particle's radius of curvature decreases. As a result, concentration gradients develop within the matrix, driving solute diffusion toward larger precipitates, which grow at the expense of smaller ones[16]. The overall result is that the total number of precipitates decreases, and the mean radius ($\bar{r}$) increases with time. By assuming volume diffusion is the rate-controlling factor, it has been shown that the following relationship should be obeyed:

$$(\bar{r})^3 - r_0^3 = kt$$

(2.4)

Where

$$k \propto D\gamma X_e \tag{2.5}$$

r_0 is mean radius initial, D is the diffusion coefficient, γ is the interfacial energy, and X_e depends on temperature. According to the equation, coarsening rate increases with increasing temperature.

$$\frac{d\bar{r}}{dt} \propto \frac{k}{\bar{r}^2} \tag{2.6}$$

So distributions of small precipitates coarsen most rapidly.

The coarsening rate is diffusion-controlled for both γ' and γ"[30].γ' follows a coarsening rate proportional to $t^{1/3}$ while γ" is a disk-like precipitate with higher lattice mismatch that grows with a rate proportional to $t^{1/2}$ [30].

2.2.3 Carbides and Borides

Many carbides and borides can form in superalloys, significantly affecting material properties. Some common examples are MC, M_6C, $M_{23}C_6$, M_7C_3, and M_3B_2, where M can be Cr, Mo, Ti, Nb, Ta, or Hf[17,18]. Most superalloys contain MC carbides, typically forming during solidification due to strong carbide-forming elements like Nb, Ti, Ta, and Hf. These carbides remain in the interdendritic region since carbide former elements segregate during solidification. The morphology also varies, for example, globuler, blocky, script, and platet[19,31,32]. The most dominant MC-Carbide in alloy 718 is Niobium-rich NbC, which forms at NbC-Eutectic temperature during solidification[33]. NbC commonly populates grain boundaries, creating a precipitate-free zone around carbide by reducing Nb content. Apart from NbC, TiC is also formed. These carbides can be observed as irregular or blocky[31].

Chromium levels of 18% or higher lead to the formation of $M_{23}C_6$ carbides, either during solidification, low-temperature aging, or in-service use. The following reaction illustrates how M23C6 carbides form at grain boundaries during aging[19].

$$MC + \gamma = M_{23}C_6 + \gamma' \tag{2.7}$$

$M_{23}C_6$ forms a film-like structure along the grain boundary that is deterious for both mechanical and corrosion properties[17,31]. $M_{23}C_6$ primary composition can be defined as $(Cr,Fe)_{23}C_6$[34].

Refractory metals like molybdenum and tungsten, when present above 6 at%, form M_6C-type carbides through the following reaction[35]. The $(Ni,Co,Cr)_4(Mo,W)_2C$, M_6C carbides may develop in the form of blocky particles or exhibit a Widmanstätten morphology[19]. Rene 41, Alloy 713, and Alloy 246 consist M_6C carbides[35].

$$MC + \gamma = M_6C + \gamma' \tag{2.8}$$

2.2.4 TCP and Laves phases

Fe, Ni, Cr, Mo, W, and Re elements in solid solution can form intermetallic phases known as topologically-close-packed (TCP) phases[36,37] after long-term temperature exposure. The resulting phases have characteristics like high atomic packing density and complex crystal structures. TCP phases precipitate in platelet structure and increase the brittleness of the alloy.

Over long-term exposure to high temperatures, W + Mo content becomes significant, leading to the early formation of TCP phases, as previously mentioned[38]. W and Mo were also reported to be very effective in forming the σ-type TCP phase[39]. Cr is another element that strongly promotes TCP formation by directly being part of

the TCP phase and altering the partitioning ratios of W, Co, and Mo, making them more favorable for TCP formation[39].

Table 2.2. TCP phases in Ni-base superalloy[18,38].

Phase	Crystal Structure	Formula	Chemical Content
σ	Tetragonal	A_2B	Ex: Cr2Ru Cr61Co39 Re67Mo33
μ	Rhombohedral	A_6B_7	Ex: W6Co7, Mo6Co7
P-Phase	Orthorhombic	$Cr_{18}Mo_{42}Ni_{40}$	-
R-Phase	Rhombohedral	$Cr_{18}Mo_{31}Co_{51}$	-
Laves	Hexagonal (C14,C36)	AB_2	$(Ni,Cr, Fe)_2(Nb,Ti)$
Laves	Cubic (C15)	AB_2	

Laves phase can be in many various crystal structures with different chemical content in different alloy systems[40]. Nb-bearing superalloys commonly form laves phases during solidification and prolonged temperature exposure[40,41]. In alloy 718, the laves phase forms in a hexagonal packed crystal structure having $MgZn_2$ (C14) lattice type[33,42]. Si, Mo, and Nb partition to the laves phase and chemical content is given in Table 2.3 [43]. This type of leaves phase is highly brittle and significantly impacts the alloy's tensile properties, reducing its notch sensitivity and low-cycle fatigue (LCF) performance[44].

Table 2.3. Alloy 718 Laves composition[43].

Elements	Ni	Cr	Fe	Mn	Mo	Nb	Si	Ti
Wt %	42.5	18	14	0.08	2.74	20.6	0.64	2.16

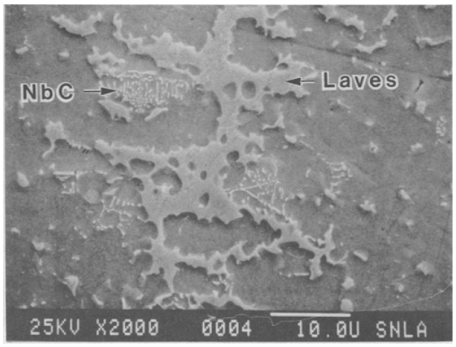

Figure 2.4. SEM analysis shows NbC and Laves phases in Inconel 718 after solidification[33].

2.2.5 Delta Phase

The Delta phase is an orthorhombic (D0a) crystal with a plate-like structure and a composition of Ni3Nb. (Lattice parameters a0 = 0.5106–0.511, b0 = 0.421–0.4251, c0 = 0.452–0.4556, [18]). δ commonly precipitates from grain boundaries 700 °C in Inconel 718 and can remain stable up to 1000 °C [46,47]. Depending on the composition and plastic deformation, the solvus temperature of the delta phase can be somewhere between 1005-1015°C [47,48]. The peak precipitation rate of the δ phase is achieved at around 900°C. The delta phase does not only precipitate from grain boundaries but also transgranularly, especially when γ" phases are present[46].

Unlike metastable γ′′, δ Phase is a stable precipitate with niobium content. However, δ Phase precipitation is much slower. Initial formation of the delta phase starts using excess niobium. However, even though the δ Phase is thermodynamically at equilibrium, unlike metastable γ" precipitate, the precipitation rate is slower, which allows γ" to form initially[45]. At prolonged temperature exposure, the δ phase precipitates and consumes γ". With the expanse of the main precipitation phase γ", mechanical properties drop rapidly, and the excessive amount of δ phase makes the material too brittle[46]. Three factors can be identified in the deterioration of mechanical properties. The first is the depletion of the main hardening phase (γ"), often observed through forming a precipitation-free zone around grain

boundaries[46]. The second factor is the increased susceptibility to crack initiation at the tips of the plate-like delta phase (δ). Finally, crack propagation along grain boundaries becomes easier. δ phase is also associated with hot cracking[46].

While an excessive amount of δ phase is detrimental to the alloy, an appropriate amount can be advantageous in thermomechanical processes. During recrystallization, the δ phase controls grain growth by Zener-Pinning the grain boundaries[49,50]. It forms through a discontinuous precipitation mechanism, nucleating at grain boundaries and growing into the grains, creating serrated grain boundaries. When δ phase formation is intentionally kept at a certain amount, this serrated structure enhances toughness and reduces notch sensitivity[51,52].

2.3 Chemistry Modifications

Much effort was put into increasing Alloy 718 maximum service temperature by modifying chemical composition to fill that gap without sacrificing the alloy's other beneficial traits. Microalloying additions such as P and B are evaluated on the effect of strength and creep properties. Phosphorus content has little to no effect on the strength and ductility of alloy 718Plus, but it can influence stress rupture life by varying its level[53]. Phosphorus does not impact the size or amount of the γ′ phase, but increasing its level reduces the amount of the delta phase[53]. Studies show that extremely low phosphorus levels can significantly decrease ductility. A higher phosphorus content improves resistance to intergranular cracking and supports the transition from intergranular to transgranular fracture modes. This effect is explained by phosphorus segregation to grain boundaries, which alters the grain boundary chemistry[54].

Alloy 718Plus was developed to improve the maximum service temperature by 55°C compared to alloy 718 by significant chemistry modifications. This improvement was achieved by reducing the iron content by 10% from the alloy 718 compositions, adding 9% cobalt and 1% tungsten, and increasing the aluminum-to-titanium

ratio[1,55]. This chemical modification resulted in altering the principle strengthening precipitate to γ′ from the γ″ phase.

As mentioned, as expected, cobalt and tungsten dissolved in γ-matrix as solid solution strengthener. However, the addition of cobalt increases niobium solubility and niobium partitioning in the matrix, reducing the availability of niobium for the γ″ phase to precipitate, which leads to a decrease in its formation in favor of γ′ formation[55].

The proportion and total content of Al and Ti elements influence the precipitation of both γ′ and γ″ phases. Reduction in the Al/Ti ratio also reduces the coarsening rate of γ′ due to the lower lattice mismatch between γ and γ′. Mechanical properties at optimum were found to have a total Al+Ti content of 4 at.% with an Al/Ti ratio of 4 at.% [55]. The amount of γ′ increases with the extra addition of Al and Ti. To make an alloy γ′-dominant, Al and Ti content sum should exceed 3 at% [55].

Meanwhile, niobium also partitions into γ′ as a result of cobalt addition, which also lowers γ/ γ′ mismatch, which is significant for the processability of 718Plus, as it slows coarsening rates and provides a broader γ′-free processing window. Similar behavior where niobium presence in γ-matrix and γ′ slowing coarsening rates and suppressing γ′ formation was also observed in alloys EI 718[56] and EI698[23].

Chemistry modification resulted in 718Plus predominantly consisting of 20-23% γ′ phase and 6.64% γ″ phase[1]. In contrast, Inconel 718 contains approximately 15% γ″ and around 4% γ′, allowing 718Plus to achieve a 55°C increase in maximum service temperature, reaching 704°C[1]. When exposed to a temperature of 760°C for 500 hours, the thermal stability of 718Plus demonstrates significant advantages compared to Waspaloy and 718 alloys. The coarsening rate of γ' precipitates in 718Plus is considerably slower than that observed in both 718 and Waspaloy alloys[57]. However, above 500 hours, more data is preferable until 4000 hours to be able to compare Waspaloy and 718Plus thermal stability. The growth rate of the η phase in ATI 718Plus is significantly slower than that of the δ phase in the 718 alloy [57].

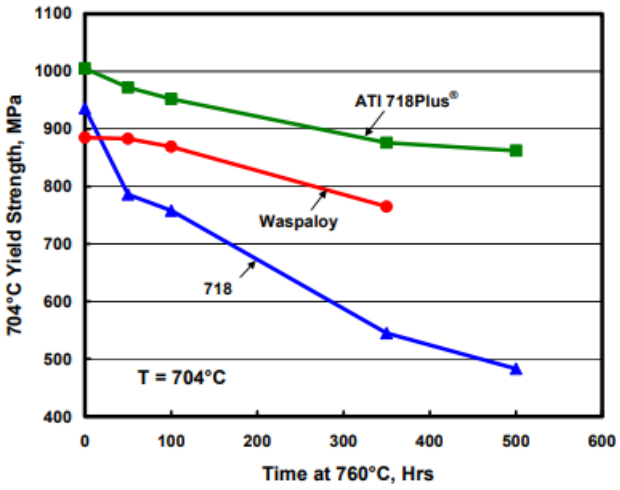

Figure 2.5. Yield strength comparison up to 500 hours of temperature exposure at 704 °C[57].

To compare weldability, continuous cooling transformation (CCT) diagrams are great tools for observing possible problems arising from the phase formed during cooling after welding. CCT diagrams are drawn using JmatPro V7 for alloy 718, 718Plus, and Waspaloy. The effects of chemistry modifications can be easily observed by comparing Figure 2.7b and Figure 2.7c graphs where γ′ becomes the first forming precipitate in 718Plus; unlike Inconel 718—the time taking the first precipitate to form is slightly reduced. However, compared with Waspaloy in Figure 2.7a, 718Plus precipitation kinetics are much more sluggish than waspaloy, which can be considered the most significant advantage of 718Plus over Waspaloy. These graphs also correlate with the observations made in Figure 2.6[55]. High aluminum and titanium content Ni-base superalloys show a cracking behavior during post-weld heat treatment. γ′ rapidly forms during heating, leading to a phenomenon known as strain-age cracking[2].

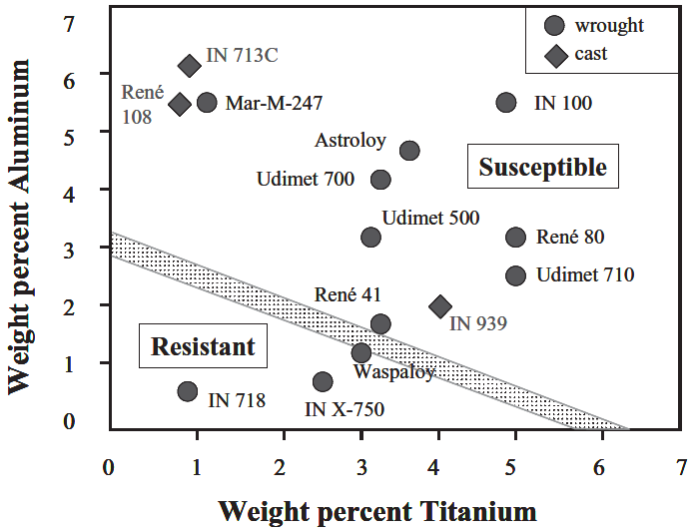

Figure 2.6. Strain-age-cracking susceptibly in various Aluminum and Titanium amounts[2].

One common practice in industry to describe weldability of Ni-base superalloy, γ′ forming elements, aluminum and titanium amounts are shown in graph as seen in Figure 2.6.

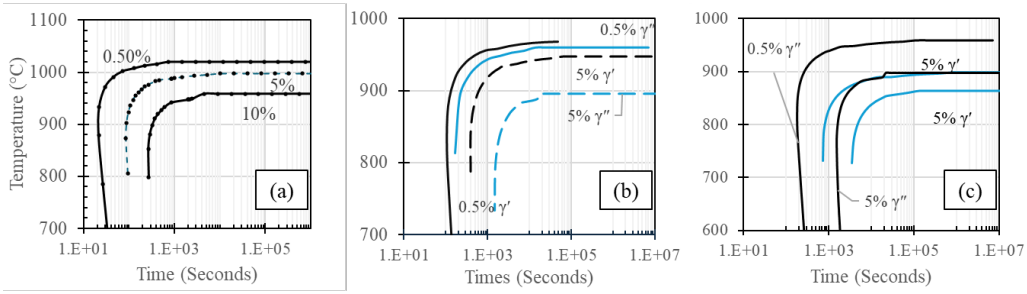

Figure 2.7. CCT diagrams drawn by JmatPro for (a) Waspaloy, (b) 718Plus, and (c) Alloy 718.

718Plus is also proved to have superior mechanical properties at 704°C compared to Waspaloy, making 718Plus is a great alternative material[1]. To date, 718Plus has been used in high-pressure compressor disks. Therefore, the AMS standard for 718Plus was published in 2012 with the code AMS5442 as bar and forged forms produced with triple melting Vacuum Induction Melting (VIM), Electro-Slag Remelting (ESR), and Vacuum Arc Remelting (VAR)[58]. Forged 718Plus proved

to be its worth at rotating parts. However, if rotating parts' maximum service temperatures are improved, static components such as combustion casings, frames, and exhaust cases may be required to operate at higher temperatures. Due to the discussed traits, alloy 718 is also used in complex static structures, often produced through casting. Since static parts are expected to endure longer operational hours, alloy 718's superior corrosion resistance, weldability, and machinability make it an ideal material choice.

Table 2.4. Chemical composition of alloy 718, 718Plus, and Waspaloy.

Alloy	Ni	Cr	Co	Mo	W	Nb	Al	Ti	Fe	C	P	B
718	bal.	19	-	3	-	5.15	0.6	1	18	0.04	0.007	0.003
718Plus	bal.	18	9	2.7	1	5.4	1.45	0.75	10	0.02	0.006	0.004
Waspaloy	bal.	19.5	13	4.25	-	-	1.35	3.00	-	0.035	0.006	0.006

2.3.1 718Plus – δ phase

In ATI 718Plus, a semi-coherent phase precipitates along the grain boundaries with a different chemistry (Ni_3AlNb) than δ, exhibiting a hexagonal crystal structure. This phase, known as the η-phase, is a variation of the typical η-phase (Ni_3Ti) found in nickel alloys. The lattice parameters were measured to be a = 0.512 nm and c = 0.836 nm[51]. A minimal amount of the δ phase exists as small strips within the η phase, detectable only through high-resolution microscopy[51]. The precipitation mechanism is similar to that of δ. In alloy 718Plus, both γ' and η can precipitate simultaneously, as seen in alloy 718 with γ" and δ phases[59]. Likewise, in alloy 718, η eventually consumes γ' after a certain point[60]. The η phase nucleates at grain boundaries but can also form in the matrix when γ' is present. The η phase has a comparable impact on the mechanical properties of 718Plus, as the main strengthening phase diminishes[61].

At early periods of nucleation, the η phase forms a granular structure along the grain boundary, which does not affect grain boundary pinning[60]. Then, the precipitate grows through the grain and transforms into a plate-like structure due to the semi-coherency[60]. As the precipitate grows, the grain boundary also slides toward the opposite side of the growth direction, distorting the linear grain boundary. The plate η serrating the grain boundary is highly effective for pinning and controlling the grain size[60]. Additionally, that serrated structure reduces the notch sensitivity as the delta phase does for alloy 718[46,60].

2.4 Alloying in Induction Melting

Alloying should be carefully planned to minimize element losses and reduce the time for melting at each addition. Key parameters in this process include melting point, reactivity with oxygen, and magnetic properties. For example, tungsten, niobium, and molybdenum have very high melting temperatures. However, these elements can be readily soluble in nickel-cobalt-iron matrix at high temperatures.

Table 2.5. Melting points of alloying elements in Alloy 718 and 718Plus.

Elements	Melting Point (°C)
Aluminum	660
Nickel	1455
Cobalt	1495
Iron	1538
Titanium	1668
Chromium	1907
Niobium	2477
Molybdenum	2623
Tungsten	3422

For accurate control of chemical composition, the most reactive elements should be added last to minimize alloying element losses. Oxidation behavior can easily be observed using the Elingham diagram Figure 2.9. Oxides of aluminum and titanium are the most stable compared to nickel, cobalt, chromium, niobium, tungsten, and

molybdenum. Therefore, these elements should be added before pouring to minimize their losses. Given their high melting temperatures, chromium, tungsten, and molybdenum can be added before the aluminum and titanium charge.

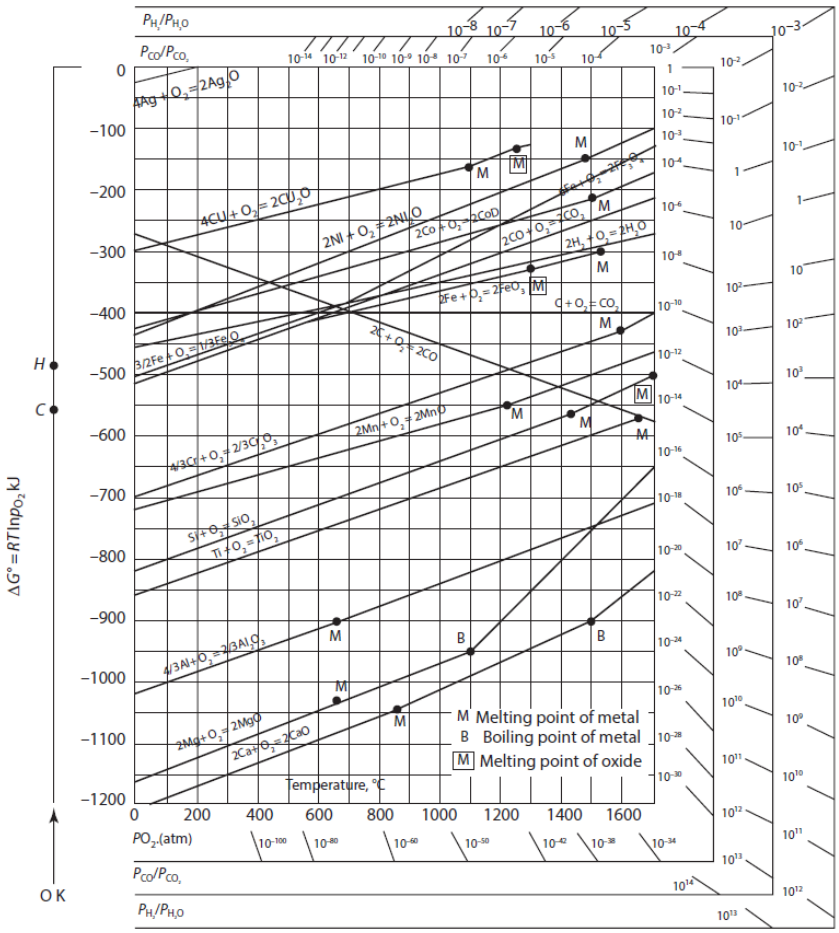

Figure 2.8 Elingham Diagram[62].

2.5 Solidification

Historically, structural components for aero engines were initially fabricated by joining smaller parts through welding, as the investment casting process was not yet advanced enough to meet the required quality standards. With the advent of vacuum casting, the production of single-piece cast components became feasible, replacing the need for welded fabrications[63]. Additinally most cast structure consist casting defects which can be repaired by welding. Therefore weldability of the alloy is an important factor in material selection of cast parts.

Typically, the complex geometry of components such as diffuses, exhausts, combustion casings, and frames make investment casting a cost-effective manufacturing method. Unlike Inconel 718, Waspaloy castings offer good material properties up to 760 °C for static components in gas-turbine engines. However, Inconel 718 shows better mechanical properties at low and intermediate temperatures. Meanwhile, regarding castability, Waspaloys tend to form hot tears more than Inconel 718. Feeding waspaloy is much more complex [64]. Therefore, weld repair after or sectioning to small pieces of the component is needed. However, as discussed before, Waspaloy is not an easily weldable alloy like Inconel 718 and 718Plus. This makes 718plus a better alternative when the operating temperature is over 649 °C, not over 704 °C. If alloys are required to be used over 704°C, extensive mechanical testing is suggested to observe the drop in mechanical properties[64].

2.5.1 Alloy 718 Solidification

Alloy 718 equilibrium liquidus and solidus temperatures were reported between 1340 - 1360°C [33,41,42,65] and 1190 – 1250°C[33,41–43,65,66], respectively in several investigations with various chemical compositions and different instrumentations. The solidification range is approximately 110-170°C, and in these temperatures, the following reactions can take place sequentially: $L \rightarrow \gamma+L$, $L \rightarrow \gamma+NbC$, $L \rightarrow \gamma+\delta$, and $L \rightarrow \gamma+Laves$[42]. The cooling rate influences Eutectic NbC

and eutectic Laves phase reactions. However, the temperature range can be described as 1280°C to 1265°C for eutectic NbC and 1160°C to 1075°C for eutectic laves [65].

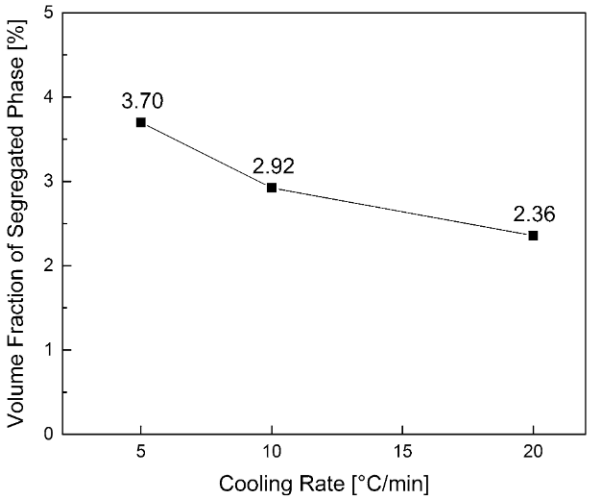

Figure 2.9. Average volume fraction of segregated phases in various cooling rates[66].

The cooling rate influences the formation of segregated phases, particularly the Laves phases. As the cooling rate increases, the Laves phase occupies less space[66].

2.5.2 Alloy 718Plus Solidification

A Differential Thermal Analysis (DTA) study for the non-equilibrium behavior of alloy 718 and 718plus[61]. 718Plus DTA analysis indicates that the liquidus temperature is 1353°C, while the solidus temperature is 1265°C[61]. In order to compare the differences, the same study also includes Alloy 718 with a liquidus of 1345°C and a solidus of 1235°C[61]. In the DTA analysis, the Laves eutectic reaction occurs at 1173°C for 718Plus and 1167°C for 718[61]. The MC eutectic reaction occurs at 1292°C for 718Plus and 1286°C for 718[61].

2.5.3 Secondary Dendritic Arm Spacing (SDAS)

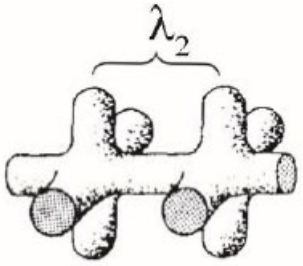

Figure 2.10. Secondary Dendritic Arm Spacing Illustration[67].

Figure 2.10 illustrates how secondary dendrites look. λ_2 is secondary dendritic arm spacing, and its formation depends on many factors discussed below.

$$SDAS = 5.5M\left(\frac{T_L - T_S}{\dot{T}}\right)^{\frac{1}{3}} \tag{2.9}$$

Where SDAS is in μm, M is a constant dependent on the material. T_L represents the liquidus temperature; T_S denotes the solidus temperature (°C); and $\dot{T}$ is the cooling rate (°C/sec). M can be found using equation (2.10) [67]. Proper instrumentation and temperature modeling with high-level control over casting can determine M using the equation (2.10). Using this method, local solidification time can be found, which can be significant for the casting validation.

$$M = \frac{\Gamma D \ln\left(\frac{C_l^m}{C_0}\right)}{m(1-k)(C_0 - C_l^m)} \tag{2.11}$$

C_0 is the initial composition, k is the equilibrium distribution coefficient, m is the liquidus slope, D is the diffusion coefficient in the liquid, and Γ is the Gibbs-Thomson coefficient[67].

In Alloy 718 solidification, an increase in cooling rate reduces the secondary dendrite arm spacing (SDAS) [68]. Study replaces T_L eutectic laves temperature. 5.5M is set to 10 for alloy 718[68].

2.6 Homogenization Treatment

When subjected to homogenization temperatures ranging from 1050°C to 1075°C, the laves phase remains undissolved even after 10 hours[69]. However, heat treatments conducted at temperatures above 1175°C, which exceed the laves eutectic point, are highly effective in dissolving the laves phase[69]. It is worth noting that eliminating the η phase is considerably more manageable than dissolving the laves phase, as the solvus temperature of the η phase is much lower[69]. Homogenization rate and effectiveness directly depend on the secondary dendrite arm spacing (SDAS), as seen in equation (2.12) below. When the solidification rate is faster, SDAS has a lower value, as discussed, which increases the efficiency of the homogenization rate.

$$t = \frac{0.47\ \lambda_{SD}^2}{D_s} \tag{2.12}$$

CHAPTER 3

EXPERIMENTAL METHODS

3.1 Raw Materials

Two types of raw materials were used in the alloying of 718Plus alloy. The first method involved alloying using entirely elemental raw materials, while the second used Inconel 718 revert, adjusting its composition by adding specific elements. The elemental raw materials included nickel, cobalt, chromium, tungsten, aluminum, and molybdenum. Niobium was added using a FeNb master alloy. Chromium and FeNb were stored as pellets, while nickel and cobalt were in slab form.

3.1.1 Batch Calculation

Three casting processes were conducted during this study. The first casting served as a preliminary trial to understand the heating and pouring procedures and to observe potential interactions between the crucible and the molten metal. In the second casting, a sand mould produced tensile specimens directly in the desired shape. Finally, the third and final casting utilized a metal mould to analyze the effects of solidification patterns and cooling rates on the resulting microstructure. Throughout the thesis, the second casting is called sand casting (SC), while the third is called metal mould casting (MC).

For the first casting, a charge consisting of 520 grams of Nickel and 70 grams of AISI 1040 steel was prepared. However, smelting was not achieved due to the low initial charge, causing excessive oxidation over a long duration.

For the second casting, revert 1960 grams of Alloy 718 used in the initial charge with 1050 grams of Nickel. The remaining elements were added in the following order:

cobalt, chromium, and iron-niobium (FeNb), followed by the simultaneous addition of molybdenum, tungsten, aluminum, and titanium.

Table 3.1. Second casting (Sand-Casting) batch calculation and aimed composition

Elements	Ni	Cr	Fe	Co	Nb	Mo	W	Al	Ti	Total
Aim (%)	Bal.	18	9.5	11	5.4	2.7	1	1.45	0.75	100
Alloy 718	1048.6	380	386	0	102.5	60	0	11	20	1960
Batch(grams)	1010.3	351.8	43.5	420	117	50	40	48	11	2050

For the third casting, the batch was prepared according to Table 3.2. The initial charge consists of 3400 grams of nickel-iron and Cobalt. For Nb, FeNb sources are used as other castings.

Table 3.2. Third casting (Metal Mould Casting) batch calculation and aimed composition.

Elements	Ni	Cr	Fe	Co	Nb	Mo	W	Al	Ti	Total
Aim (%)	Bal.	20	9	9	5.5	2.8	1	1.7	1	100
Batch(grams)	2500	1000	326	450	416.7	140	50	85	50	5000

3.2 Phase Predictions

In this thesis, JMatPro Version 7 was used to predict the potential phases formed during solidification and homogenization heat treatment. Variations in chemical composition were input into the model to compare the predictions with the observed microstructure. SDAS values were provided as input to the homogenization module using the resulting microstructure to estimate the chemical composition profile after the homogenization process.

The Scheil-Gulliver approach, used in thermodynamic modeling, allows for predicting the thermophysical properties of alloys, including nickel-based superalloys, during solidification. This method assumes that solute diffusion in the

solid phase is negligible and that diffusion in the liquid phase is fast enough to be considered complete. It also assumes that the liquid-solid interface remains in thermodynamic equilibrium[70]. The model predicts segregation under extreme conditions and identifies possible phases that can form during solidification, supported by the CALPHAD method[70].

After solidification, solid-state transformations take place during cooling, resulting in new phase formation. Solidification cooling diagrams presented combine Scheil-Gulliver cooling and subsequent solid-state transformations[70]. The solidification cut-off is defined at a weight ratio of 0.02.

3.3 Melting Method

The smelting is conducted in an Inductoterm Induction Furnace. The contaminant from the open atmosphere is reduced by applying argon pressure by placing a cap with a gas tube directly from above. The tube is attached to an Argon gas tank. A wool thermal blanket is placed between the cap and the crucible to shield the cap from radiating heat. This setup also minimizes heat loss and helps reduce operation time. The water-cooled jacket surrounding the induction melting system can be seen as having black sleeves. The induction furnace setup with an argon gas cap is illustrated in Figure 3.1.

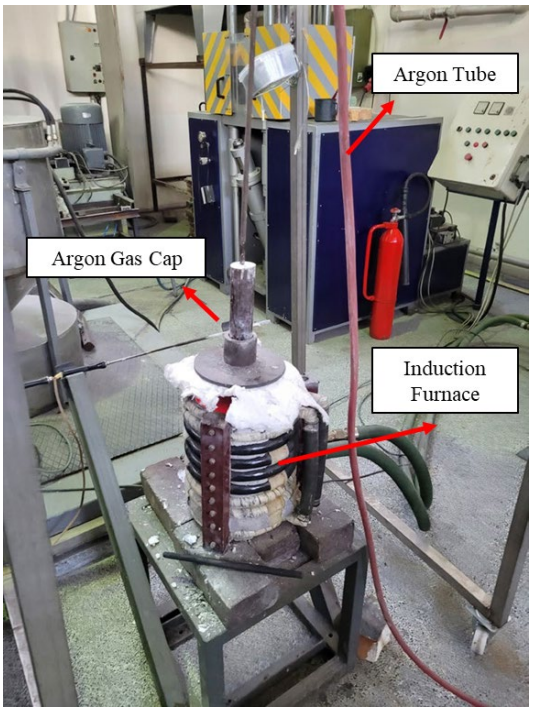

Figure 3.1. Smelting setup in an induction furnace. Argon gas cap is placed on top of the crucible, holding the tube where argon flows.

3.3.1 Crucible

In the study, a Kiln-Graphite type crucible was used. Crucible dimensions were chosen based on the total batch amount to minimize heat loss and reduce thermal stress on the crucible. Since Ni-base superalloys are found to be highly erosive for these crucibles, the inner walls of the crucible were coated with hexagonal Boron Nitride (hBN) as a liner to address this. hBN powder was mixed with sodium silicate and water. The mixture was applied to the inner wall with a brush and sintered in a furnace. The crucible with coating is shown in Figure 3.2.

Figure 3.2. Kiln-Graphite crucible, where the inner wall is coated with hBN and serves as a liner.

3.4 Moulds Geometry and Materials

This study used two types of moulds: a sand mould, designed to produce tensile test specimens directly, and a metal mould, shaped to cast slabs.

3.4.1 Sand Mould

In the initial castings, a sand mould was used to directly produce four tensile test specimens. Small risers were placed at both ends to feed the specimens. The Alkafen mould was cured using an alkali phenolic resin. Silica sand was mixed with the resin and shaped into the desired geometry, followed by curing with carbon dioxide gas. The CO_2 acted as a catalyst, initiating the polymerization reaction that hardened the mould. After curing, the moulds were inspected for structural integrity and surface quality. Sand mould can be observed in Figure 3.3.

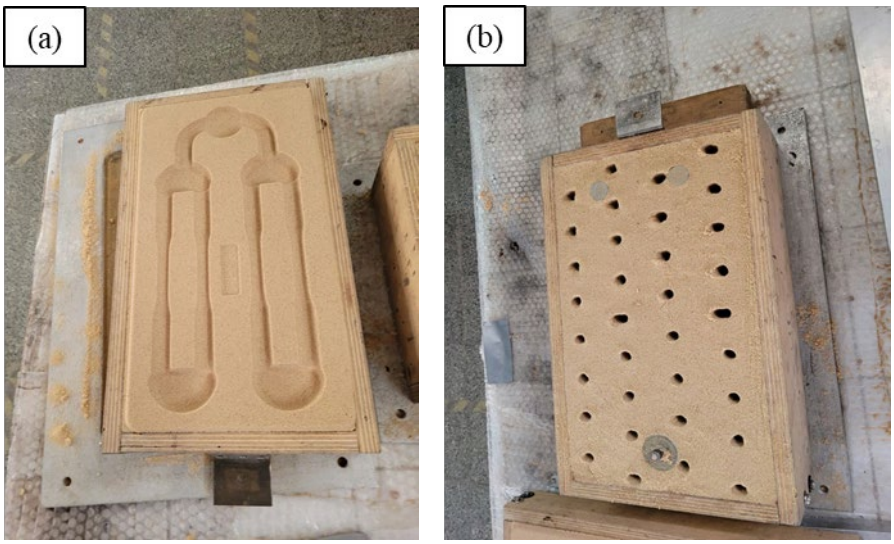

Figure 3.3. A sand mould is used for specimen production. (a) cope (b) mould after hardening using CO2.

3.4.2 Metal Mould

A metal mould equipped with a side riser is used in the third casting process. Instead of directly producing specimen shapes, a slab geometry is cast. Test specimens are then extracted from the slab. To prevent metal contact with the mould surface, the walls of the metal mould are coated with a zirconium-silicate-based solution applied using a brush and allowed to dry.

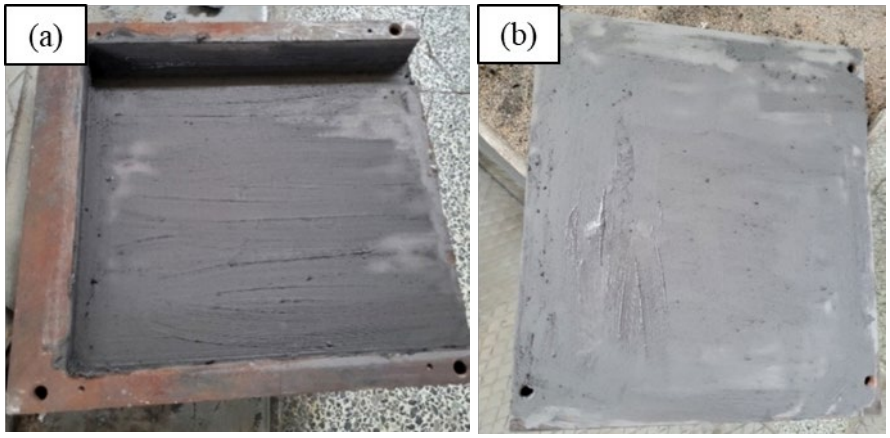

Figure 3.4. Metal mould with zirconium silicate coating. (a) the mould side with the riser feature. (b) the cap side of the mould.

The mould setup can be seen in Figure 3.5. Metal plates are secured using two C-clamp holders. The mould is preheated before pouring the liquid metal to minimize thermal shock and rapid cooling. A flame torch is positioned at the top of the mould for heating, and the temperature is monitored using a pyrometer. The square cavity that is seen on the side of the mould in Figure 3.5 is where metal is poured from. This cavity also functions as a riser and solidifies the last.

Figure 3.5 Metal mould is held by two holders. A flame is heating up to metal from the above.

The coating is beneficial in preventing the metal from fusing into the mould walls. After casting, simply releasing the clamps is enough to remove the slab from the mould. The alloy is then allowed to cool naturally in the air.

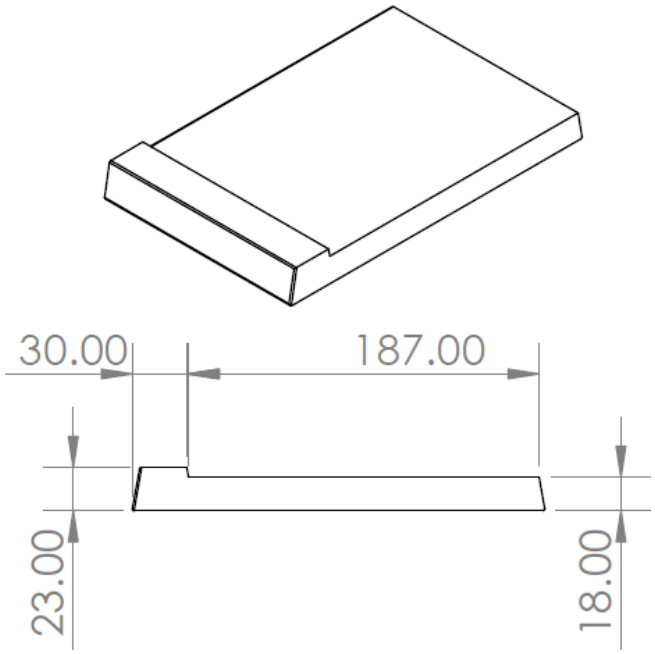

Figure 3.6. Slab geometry dimensions cast with a metal mould (in millimeters).

Slab model dimensions are shown in Figure 3.6. The thickest section acts like a riser for the slab, and pouring takes place from that location. The slab thickness is 18 mm, and the width is 140 mm.

3.5 Heat Treatment

For homogenization, solutinization, and aging, the same box furnace in Figure 3.7 is used, which can reach temperatures up to 1200°C.

Figure 3.7. Box furnace used for homogenization, solutionizing, and aging heat treatments.

Two different homogenization treatments were tried. The expected dissolution of phases was simulated using JmatPro V7. The alloy was held at 1100 °C for eight hours in the first trial, and water was quenched. In the second trial, a two-step homogenization treatment was picked to avoid possible incipient melting. After homogenization, alloys were water quenched.

1. Homogenization: 1100 °C for 8 hours
2. Homogenization: 1100 °C for 2 hours + 1125 °C for 10 hours

After the second homogenization heat treatment, the subsequent heat treatment process is applied.

- Solution Treatment: Heated to 968 °C, held at 968 °C for 1 hour, and then water-quenched.
- Aging Heat Treatment: Heated to 788 °C and held for 8 hours, then cooled to 704 °C at a 42 °C/hour rate. Once at 704 °C, the alloy was held for 8 hours before being air-cooled to room temperature.

Aging parameters are similar with industrial applications. The alloy was held at 788 °C for 2 hours, and the furnace was cooled to 704°C at a 42°C/hr rate. Then, the alloy held an additional 8 hours at 704°C and cooled naturally in air.

3.6 Sample Preparation

Castings in sand moulds were in tensile test specimen shape. Only surface defects were removed before testing by machining. The specimens from the slab were taken by cutting and machining.

3.6.1 Post Processing of Slab Castings

AMS 2773 and AMS 2774 are heat treatment standards that outline standard practices and acceptance criteria for each heat treatment stage in cast and wrought Ni- and Co-based superalloys. This specification suggests that, above 871°C, the surface layer shall be removed 0.21 mm, especially when a protective atmosphere is unsuitable [71,72]. To remain in safety, the slabs are cut through square bars to be put into heat treatment furnaces. After solution treatment, tensile test specimens are machined by using a lathe.

3.6.2 Metallographic Specimen Preparation

Metallographic specimens are taken from the holders of tensile test specimens. Due to the difficulty of cutting the alloy, most of them had poor surface quality. All metallographic specimens are mounted in Bakelite to provide a stable and durable base for grinding, polishing, and microscopic examination. The grinding of metallographic specimens started with 240 grit and continued sequentially through 400, 600, and 800 grit, with each step performed for 20-30 seconds under flowing water. Final grinding took place at 1200 grit and was repeated three times before polishing. The metallographic specimens were polished using Al_2O_3-based solutions, progressing from 3 microns to 1 micron and concluding with a final polish at 0.3 microns. Each polishing step lasted 3 minutes.

Several etchants were tested for as-cast, homogenized, solutionized, and aged-conditioned specimens. Gliceria and Waterless Kalling, also known as Kalling 2,

were used in homogenized conditions. Both etchants were applied by immersion. The compositions of the etchant can be found below.

- Gliceria: 15ml HCl + 20cc Glycerol + 5ML HNO_3
- Waterless Kalling (Kalling 2): 5 gr $CuCl_2$ + 100cc HCl + 100cc Ethyl Alcohol

3.6.2.1 Optical Microscopy

Two optical microscopes were utilized for microstructural evaluation. A Huvitz-brand optical microscope was used to compare microstructural changes in each process. A SOIF XJP-6A optical microscope was also used to measure secondary dendritic arm spacing (SDAS) for slab casting. The measurements were analyzed using Material Plus software and ImageJ.

To evaluate the effectiveness of homogenization, solution treatment, and aging, micrographs captured using a Huvitz optical microscope were processed through binary segmentation to create clear contrasts and calculate area ratios. The AI tool ChatGPT was used for image analysis regarding binary segmentation and area measurements.

3.6.2.2 Scanning Electron Microscopy

Specimens were examined using SEM to identify phase composition, evaluate segregation following solidification, and assess the effectiveness of homogenization through Energy Dispersive Spectroscopy (EDS). Backscatter (BSE) and secondary electron (SE) imaging techniques were critical for studying nickel alloys, as they effectively reveal the segregation of essential alloying elements like Nb, Al, and Ti. EDS also supported BSE images to differentiate contrast differences. JEOL JSM-6400 Scanning Electron Microscope used.

3.7 Mechanical Testing

Sand mould casting produced four tensile test specimens as in Figure 3.8. The process allocated two specimens for machining trials and reserved two for tensile testing. Testing focused on the homogenized condition of these specimens to evaluate the solution alloy's behavior without hardening effects.

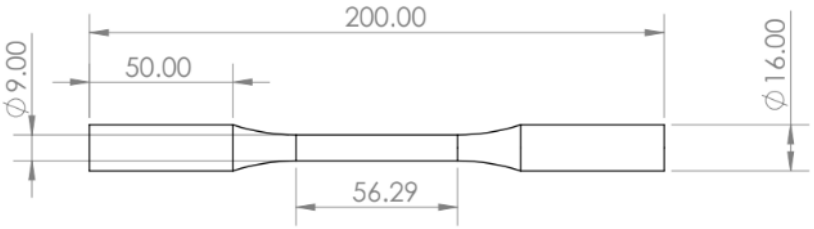

Figure 3.8. Sand mould casting tensile specimens

Metal mould casting produced two tensile test specimens prepared through cutting and machining. Tensile tests were then conducted on both specimens in aged conditions—an Instron 5985 instrument was used. The rate of tension is set to 1mm/min.

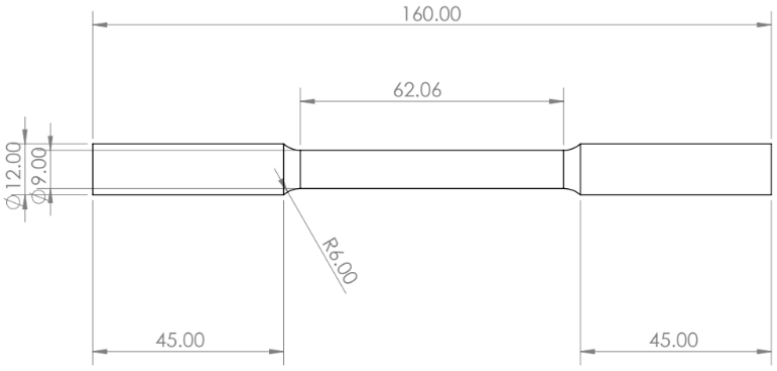

Figure 3.9. Tensile Test Specimen dimensions taken from metal mould casting.

Figure 3.9 is a drawing of a tensile test specimen. The 1mm/min drawing rate in the tensile test corresponds to a 0.0167 mm/mm/min strain rate.

CHAPTER 4

RESULTS AND DISCUSSION

4.1 Alloy Modeling

4.1.1 Equilibrium Phase Diagram

Two-phase distribution diagrams of 718Plus are prepared using JmatPro, as shown in Figure 4.1. Figure 4.1a shows phase distribution when the stable phase delta freezed. Figure 4.1b shows the equilibrium phase distribution diagram. When delta phase formation is frozen, the γ″ phase can reach up to 4.96% at 700°C, while the γ′ phase is approximately 20.50%. Delta and γ' solvus temperature is determined to be 1009 °C and 973°C. Equilibrium liquidus and solidus temperatures are 1350.41 and 1262.45°C, respectively.

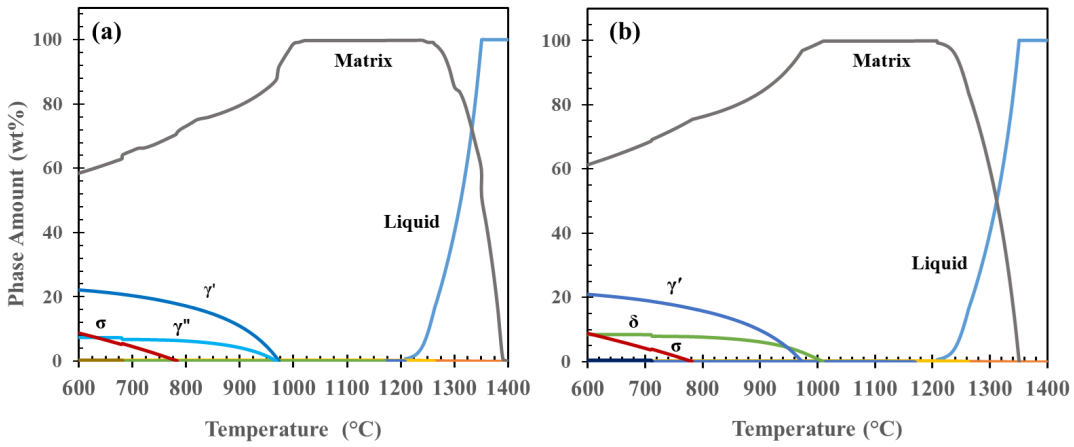

Figure 4.1. 718Plus equillibrium phase distribution diagrams. (a) Delta phase is freezed and not included. (b) All phases are included.

4.1.2 Solidification

JmatPro V7 Scheil modeling estimates what phase forms and validates the tool for future use. The solidification cut-off amount is set to 0.02wt%, corresponding to around 1116 °C temperatures, as seen in Figure 4.2. Solidification (L → γ+L) starts at 1352°C. During solidification, the liquid metal sequentially forms the gamma, MC-type carbides, Laves, and delta phases. MN-type nitride is insoluble and starts to create due to nitrogen reacting with titanium even before pouring. The eutectic L → γ+NbC reaction takes place at 1244 °C while the laves-eutectic (L → γ+Laves) point is at 1152°C. Al, Ti, Mo, and Nb elements are not readily soluble in the initially formed gamma matrix phase, and these elements remain in the interdendritic region.

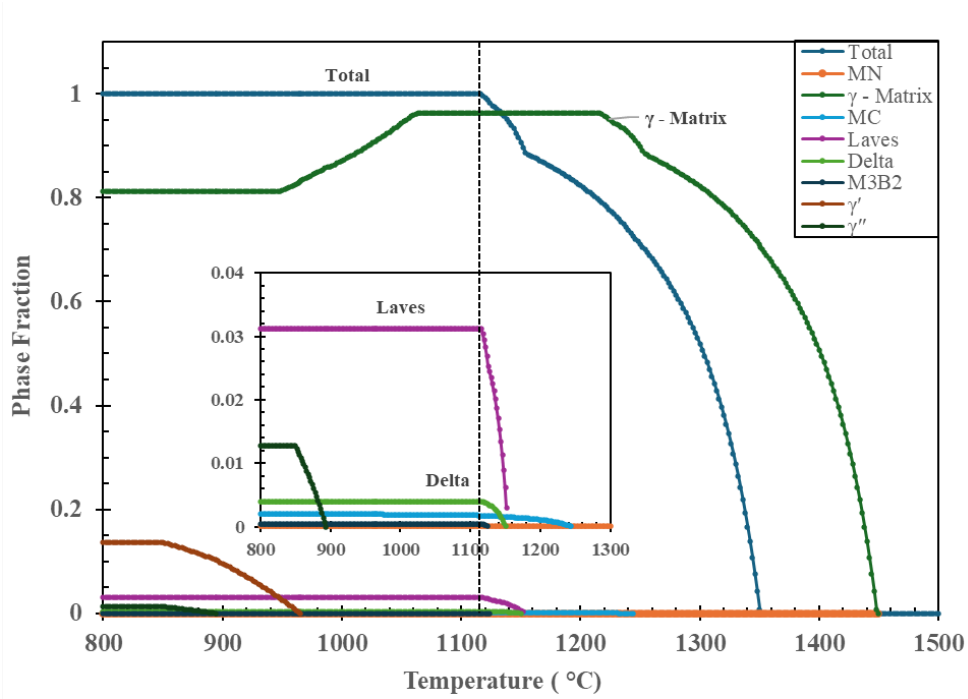

Figure 4.2. 718Plus phase amount modeled by solidification module JMatPro V7.

Chromium, Tungsten, Molybdenum, Cobalt, and Iron partition the dendritic region and remain in the matrix phase. MC-type carbides and delta phases are niobium-rich. Therefore, these phases are commonly placed in the interdendritic region.

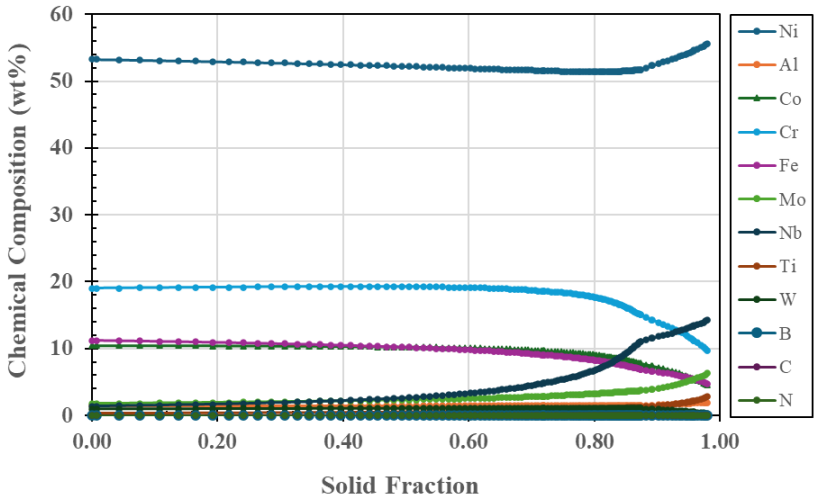

Figure 4.3 Variation in the chemical composition of γ-matrix during solidification.

Figure 4.2 shows γ matrix chemical composition evolution as solidification takes place. Where the solid fraction of 0.0 corresponds to the liquidus temperature. The overall chemical composition of the matrix phase at liquidus temperature and the end of freezing is listed in Table 4.1.

Table 4.1. JMatPro estimation of matrix phase chemical composition at liquidus temperature and at when 100% solid present during solidification.

Phase	Ni	Co	Cr	Fe	Mo	Nb	W	Al	Ti
γ – Matrix (L)	53.3	10.5	19.0	11.2	1.8	1.4	1	1.5	0.4
γ – Matrix (S)	55.6	4.6	9.65	4.8	6.3	14.2	0.27	1.85	2.85

Meanwhile, average phase compositions are listed in Table 4.2. The Laves phase was estimated to be enriched in Nb and Mo compared to the equilibrium matrix phase composition. The MC phase is predominantly Nb-rich, containing approximately 85% Nb. TiN is anticipated to consist of 75–76% Ti.

Table 4.2. Phase average chemical composition (wt%) estimated by JmatPro.

Phase	Ni	Co	Cr	Fe	Mo	Nb	Ti	C	N
Laves	33.41	6.12	15.69	7.21	2.94	33.36	-	-	-
Delta	57.94	5.11	-	-	-	33.11	-	-	-
MC	-	-	-	-	-	85.95	3.54	9.95	0.03
TiN	-	-	-	-	-	1.83	75.90	0.70	21.38

4.2 Castings

The first casting attempt was unsuccessful due to an insufficient batch size for melting using induction heating. Consequently, a minimum batch limit was established for subsequent castings. Additionally, significant erosion was observed on the kiln-graphite crucible during this initial trial. A metal bar was used to mix the liquid, but it was lost in the molten metal.

An argon gas cap was utilized to minimize atmospheric reactions and radiation cooling to prevent similar issues encountered during the first casting. A protective coating was also applied to the crucible walls to prevent its degradation. Metal bars for mixing were also coated with hBN.

Sand and metal castings were presented in Figure 4.4 and Figure 4.5, respectively. Shrinkages on the risers were readily observed.

Figure 4.4. Sand casting product with runners and risers attached.

Figure 4.4 was the geometry taken directly by casting.

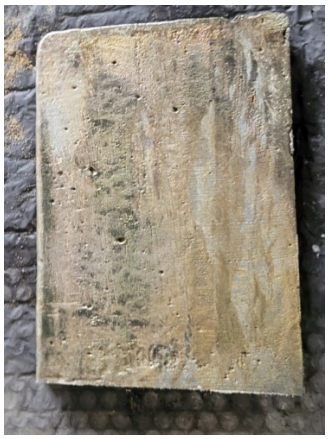

Figure 4.5. Metal castings in the shape of a slab. A band saw cuts the riser side.

The produced slab is in Figure 4.5. Many dimples and long marks are readily observable on the surface. This poor surface quality is attributed to the coating on the metal mould and the gas escaping along the mould walls. The riser is removed using a band saw, and shrinkage cavities remain in the riser. Meanwhile, shrinkage in the slab only remained on top and was removed by using a band saw again. The surface feature remained insignificant since the specimen was extracted from the center. However, the final machining was finished after homogenization and solution treatment, both of which were above 871°C.

Risers and runners were easily separated from the casting produced from sand mould. However, casting from the metal mould was challenging even though the alloy was machined in homogenized and solution-treated conditions. During the process, five tooltips broke. Meanwhile, slicing the slab spent two band saws. Additional details on the topic are provided in the following sections.

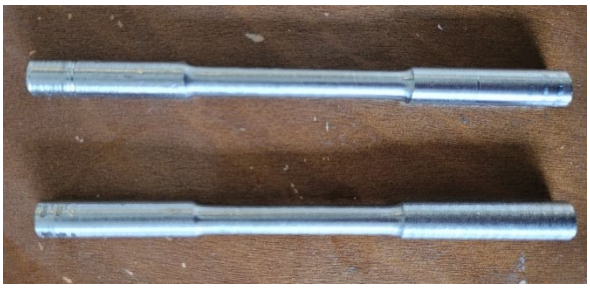

Figure 4.6. Tensile specimens from metal mould castings after machining.

4.3 Chemical Analysis

Sand casting chemical composition is presented in Table 4.3.

Table 4.3. Chemical analysis of sand casting.

Elements	Si	Cr	Mo	Nb	Ti	Al	Co	W	Fe	Ni
Weight Pct (%)	0.087	18.13	2.55	5.058	0.752	1.164	12.6	1.1	9.72	48.78

The batch is modified according to the sand casting results. Considering the losses in aluminum, the amounts of aluminum and titanium are set at the maximum possible level. The niobium amount is increasing by 0.1%, and the chromium level is rising to 20%. The cobalt and Iron levels were found to be more than charged in the first casting. It is 0.22% for iron, but the value reached 2.1% for cobalt. Therefore, these elements are reduced to 9%.

Table 4.4. Chemical analysis of metal mould casting.

Elements	Si	Cr	Mo	Nb	Ti	Al	Co	W	Fe	Ni
Weight Pct (%)	LOD	19.2	2.93	5.7	1	1.52	9.2	0.81	8.9	50.46

The tungsten level approached the minimum allowable limit in the third casting despite the batch calculations targeting a 1% composition. Meanwhile, molybdenum amounts have been increased, which usually behaves similarly to tungsten. The

reduction of tungsten is possibly caused by the short holding time of tungsten in melt. The tungsten melting point is too high and typically dissolves into the liquid. The suggested solution to this problem is adding tungsten with molybdenum earlier and increasing the time between tungsten addition and pouring to provide enough time for dissolution.

The casting records and sequence of element addition are listed below. The batch was prepared by combining Nickel, Iron, and Cobalt. This was followed by the addition of refractory elements, with Tungsten being the last refractory element added. Aluminum and Titanium were added just before pouring to prevent oxidation losses of these elements.

T-0 (Initial Charge): Nickel-Iron-Cobalt (3400 grams charged)
T-12:45: Chromium added
T-13:40: Iron-Niobium (FeNb) added
T-15:16: Molybdenum added
T-17:55: Tungsten added
T-20:58: Aluminum-Titanium added
T-28:54: Pouring

4.4 Mechanical Testing

Sand castings in homogenized condition tensile test results are presented in Table 4.5. Test results show good ductility with 19% and 26% elongation.

Table 4.5. Tensile test results of sand castings (SC).

Sample	Yield Stress (Offset 0.2%) (MPa)	Ultimate Tensile Stress (MPa)	Elongation (%)
SC Sample 1	328	504	19%
SC Sample 2	427	600	26%

In literature, tensile tests were conducted for several alloy 718s in homogenized condition. These tests demonstrate a yield strength of 250-270 MPa and an ultimate tensile strength (UTS) of 520-540 MPa under various heat treatment conditions between 1070°C and 1120°C with different holding times[73]. These results are comparable to the sand casting results for 718Plus in this thesis. Regarding elongation, the literature reports values of 60-75% [73], whereas in this study, elongation is 19% and 26%, showing significant variation.

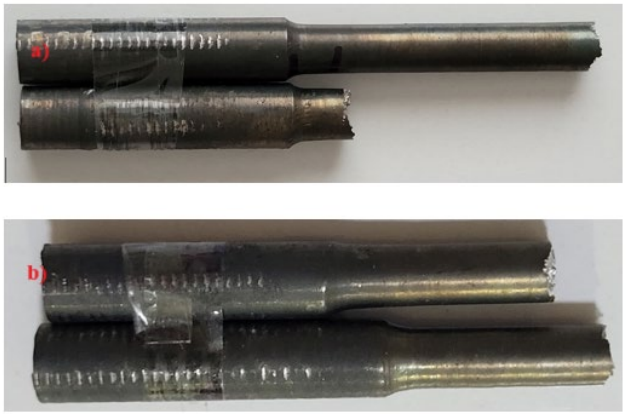

Figure 4.7. Fracture location of metal mould castings tensile test. (a) Sample 1, (b) Sample 2.

After aging, the alloy exhibits a brittle behavior. This brittleness is closely linked to the remaining Laves phase content in the material's microstructure after solidification and heat treatments.

Table 4.6. Tensile test results of metal mould castings (MC).

Sample	Yield Stress (Offset 0.2%) (MPa)	Ultimate Tensile Stress (MPa)	Elongation (%)
MC Sample 1	-	839	0.70%
MC Sample 2	722	802	0.59%

Figure 4.8. Sample 1 fracture surface after tensile test.

Both samples in Figure 4.8 and Figure 4.9 have shiny fracture surfaces. Dark areas are located on both. Sample 1 dark spot remained at the center. The next one is set to be on the edge. Fracture surfaces exhibit a brittle fracture.

Figure 4.9. Sample 2 fracture surface after tensile test.

4.5 Microstructure Evaluation

In this study, an extensive evaluation of the microstructure was conducted using optical microscopy and scanning electron microscopy. The findings for each casting were presented individually, and the results were compared with metal mould castings through detailed image analysis.

4.5.1 Sand Castings Microstructure Evaluation

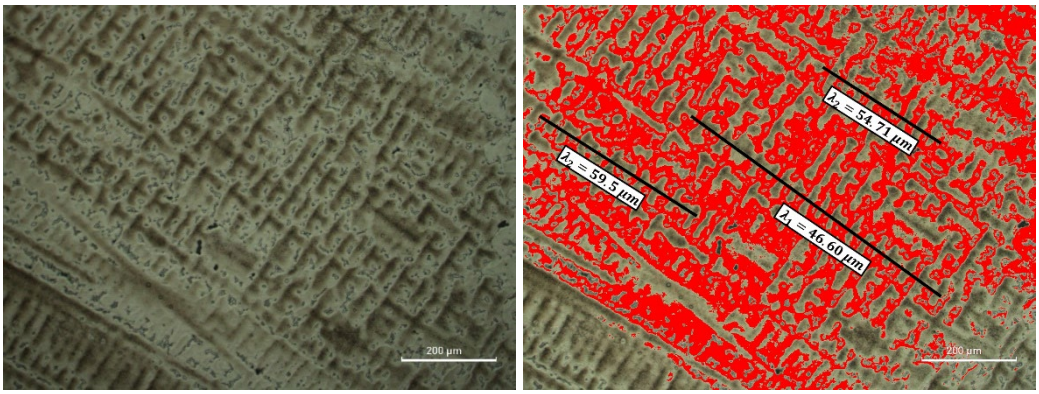

Figure 4.10. As-cast microstructure of sand castings. Kalling 2 etchant used. 360X magnification.

The specimen was immersed in Kalling 2 for three minutes, resulting in a dark coloration in the dendritic regions. Secondary Dendritic Arm Spacing (SDAS) was measured manually using Image J software's scale bar. The branches at the center were picked for measurement to avoid microscope focus problems. In Figure 4.10, the black lines represent the branches used in the analysis. With the Image J software, the dark areas were highlighted in red. The uncolored regions represent the interdendritic areas. The SDAS values given in Figure 4.10 are averages of one branch. Then, the overall SDAS value is compared in Table 4.9 with the average SDAS value coming from metal mould.

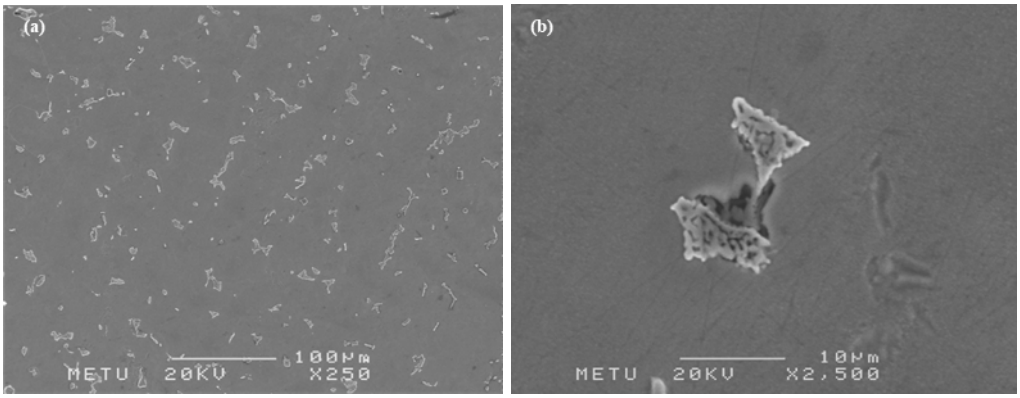

Figure 4.11. As-cast condition sand castings evaluation under SEM (a) x250 magnification (b) laves phase in 2500X magnification. Kalling 2 etchant used.

In Figure 4.11, laves-like structures formed in a pattern, as seen in x250 magnification. EDX analyses were performed on these structures and reported in Table 4.7, which appear rich in Nb. Aluminum, titanium, and niobium elements have low solubility in γ- matrix and preferentially segregate through interdendritic regions. Therefore, the phase of these elements as constituents was expected to be highly populated between dendritic regions, as seen in the case of laves formation.

Table 4.7. Chemical composition (wt%) of laves phase in Figure 4.11b.

Elements	Si	Ti	Cr	Fe	Co	Ni	Nb
Weight Concentration (%)	0.73	0.59	12.06	6.68	12.54	39.21	28.19

Figure 4.12 shows the BSE view of sand castings in as-cast conditions without heat treatment. Heavy elements like niobium look brighter, while light elements like aluminum and titanium are observed to be darker. The solid white structures were identified as NbC, with niobium as the primary constituent. This high niobium content causes these structures to appear brighter compared to others.

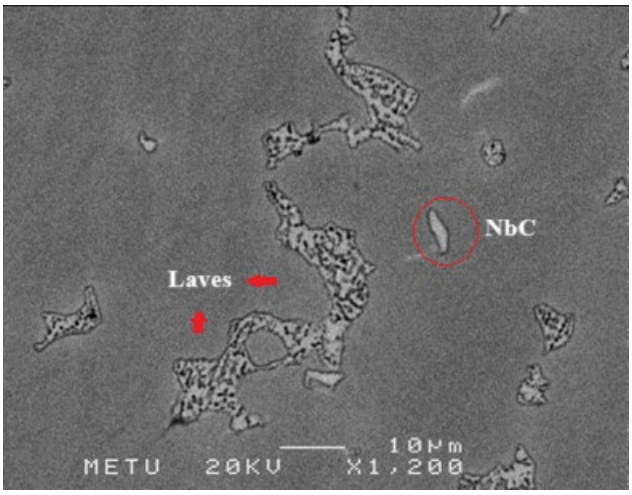

Figure 4.12. BSE view of the laves phase from sand casting in as-cast condition. Kalling 2 etchant is used.

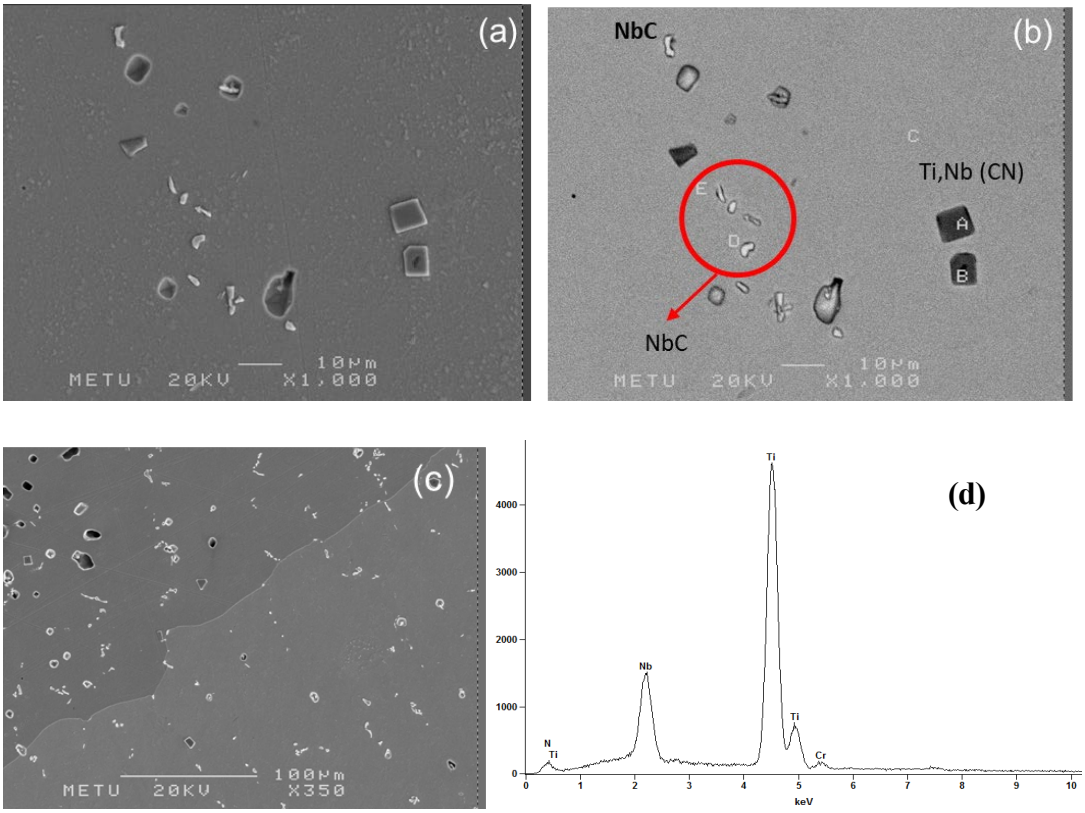

Figure 4.13. SEM microstructure of homogenized 718Plus alloy: (a, c) SE images, (b) BSE image, and (d) EDS analysis of structure B in (b). Etchants used: Glyceregia for (a, b) and Kalling 2 for (c).

In Figure 4.13, the SEM microstructure of the sample was homogenized for 8 hours at 1100°C 718Plus. Glyceregia etchant was applied to the specimens in Figure 4.13a and Figure 4.13b. In image Figure 4.13c, the microstructure is revealed using Kalling 2 etchant. Square dark structures were rich in titanium with a 75% ratio, exhibiting characteristics of titanium-nitrides (TiN) formed before and after starting to solidify of melt. A darker structure appears inside the cubic TiN phase coded with the letter "B" in Figure 4.13b. EDS analysis showed that Al and Ti enriched the phase, indicating an oxide inclusion that acted like a nucleant for TiN. Oxide inclusions such as magnesium and aluminum can act as nucleants for TiN during solidification[74]. Figure 4.13b, bright precipitates in the BSE image were niobium-rich, and EDX analysis from phase D and phase E reported 82.04% and 69.89% Nb,

respectively. Table 4.8 presents the chemical content of the discussed phases in Figure 4.13b.

Table 4.8. The chemical content of phases in Figure 4.13b.

Elements	Al	Ti	Cr	Fe	Co	Ni	Nb	Si
Phase A	-	75.92	2.16	-	-	-	21.92	-
Phase B	12.16	63.74	1.97	-	-	1.88	20.26	-
Phase C (Matrix)	0.77	0.45	19.20	11.02	11.92	50.83	5.56	0.24
Phase D	-	4.81	3.37	1.75	1.69	6.33	82.04	-
Phase E	-	4.22	5.40	3.29	3.34	13.85	69.89	-

Table 4.8 EDX analysis is also taken from the matrix phase, indicated with C. Iron and Cobalt levels are higher values. Meanwhile, aluminum content is 0.77 wt%, which is 0.4% lower than XRF chemical analysis in Table 4.3.

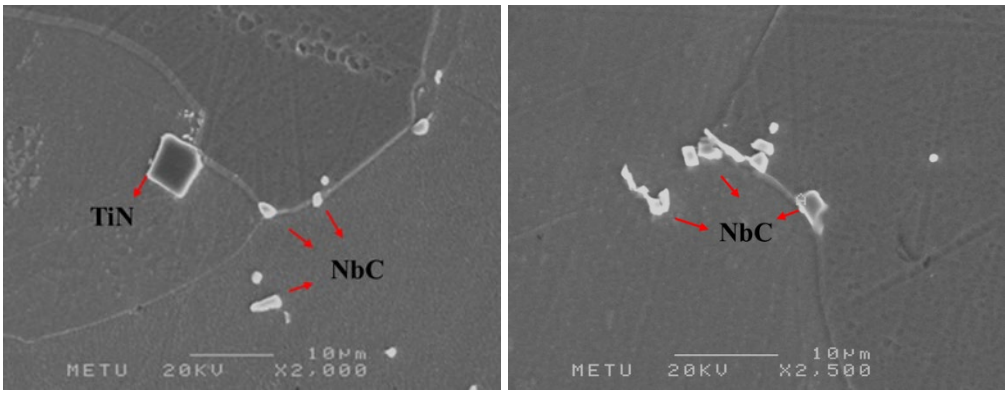

Figure 4.14. Grain boundary view of sand castings in homogenized condition under SEM. Kaling 2 etchants were used.

Figure 4.14 shows phases located in grain boundaries. EDX analysis showed that bright white structures are NbC, and no $M_{23}C_6$ or M_6C type carbides were observed in homogenized conditions.

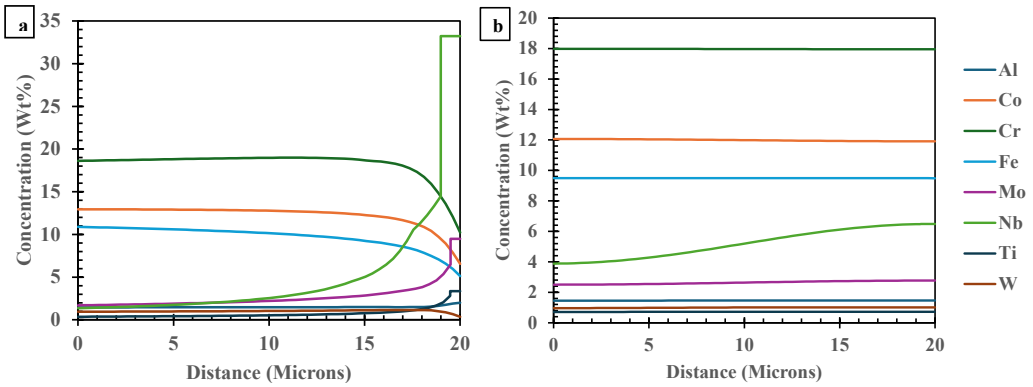

Figure 4.15. Homogenization modeling using JMatPro V7 for sand casting. (a) Segregation at time 0. (b) Segregation after 8 hours.

The JmatPro model shows nearly complete homogenization after 8 hours of heat treatment at 1100°C in Figure 4.15. Only Nb exhibits slight variation along the dendritic arm spacing. This behavior is also supported by the images taken from SEM in Figure 4.13 and Figure 4.14. No Laves phase remains in the microstructure. However, numerous NbC particles are present in both the matrix and along the grain boundaries. Other carbide structures, such as $M_{23}C_6$ and M_6C, were not observed.

4.5.2 Metal Mould Castings Metallographic Evaluation

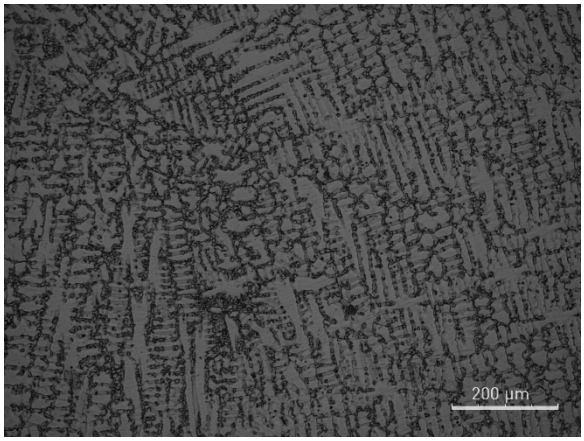

Figure 4.16. As-cast condition of metal mould casting in x360 magnification under optical microscope from central area.

The dendritic solidification was observed clearly in Figure 4.16. The dendritic structure formed finely due to the mould material. For dendritic arm spacing measurement. Following figures were used.

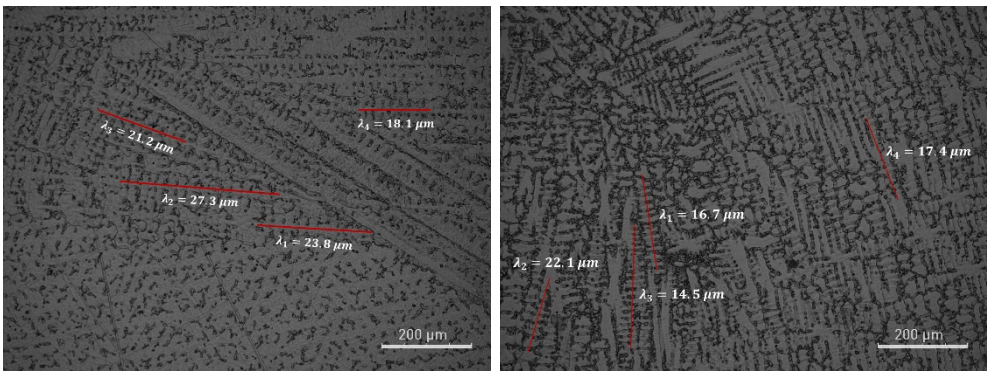

Figure 4.17. Manual SDAS measurements from metal mould casting. **Left:** Dendritic pattern near the mould. **Right:** Dendritic pattern from the central region.

Figure 4.17 shows manual SDAS measurements from several dendritic arms. Near the mould wall, the dendritic pattern is oriented toward the right. In the central area, newly formed dendrites grow in multiple directions, exhibiting shorter SDAS. Compared to the sand castings, the SDAS is significantly shorter in the metal mould casting. Table 4.9 shows average secondary dendritic arm spacing for both casting. These results show a similar trend to previous studies with alloy 718, showing that an increase in cooling rate leads to a decrease in SDAS [68].

Table 4.9. Secondary dendritic arm spacing (SDAS) measurement of each casting.

	Sand Mould	Metal Mould
Average SDAS (µm)	53.6	19.5
Min (µm)	35.0	10.9
Max (µm)	67.8	32.0
Std Dev	8.7	4.41

Estimated effect of 19.5 µm over homogenization is illustrated in Figure 4.18. At T0 NbC and Laves phase are present in the model. The homogenization process is carried out in two steps: first, at 1100°C for 2 hours, followed by heating to 1125°C

and holding there for 10 hours. The graph displays three curves: T0 is represented in blue, T0+2 hours after the 1100°C treatment is shown in orange, and the results of the final step, T12, are depicted by the green curve. For simplicity, only Nb concentration was considered, as the highest degree of segregation was observed for Nb.

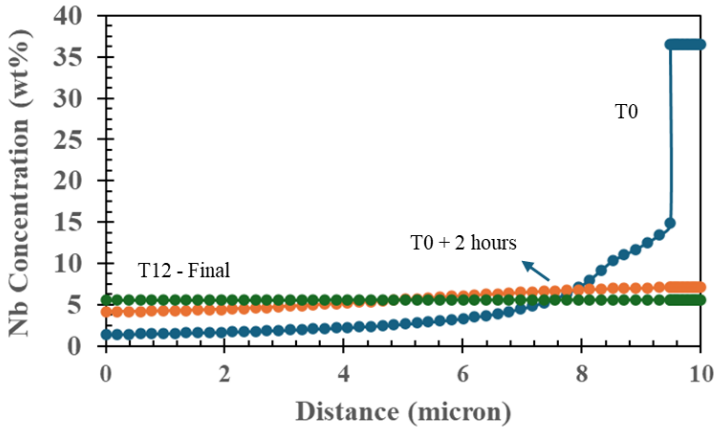

Figure 4.18. The Effect of Homogenization on Nb in Metal Mould Casting Based on JmatPro Analysis.

Figure 4.18 indicate that nearly complete homogenization can be achieved after 12 hours of heat treatment conducted in two steps. During the first step, Nb-rich phases are expected to dissolve.

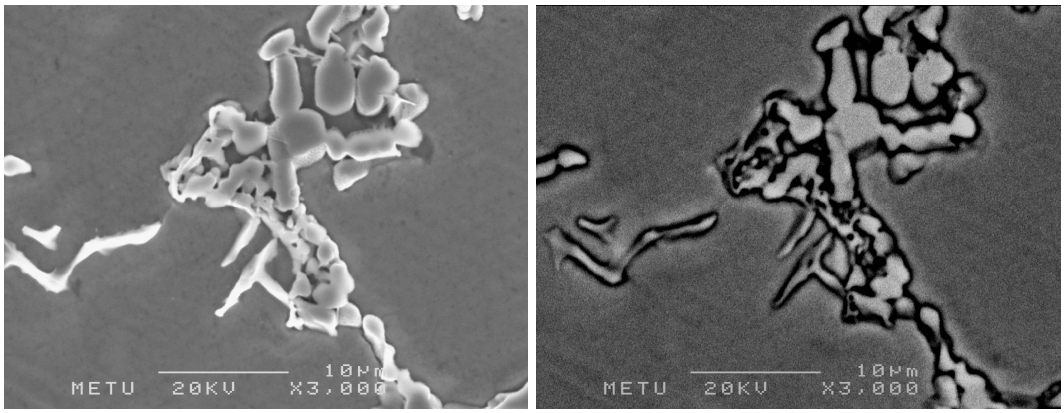

Figure 4.19. SE and BSE view of metal mould casting in the as-cast condition.

Figure 4.19 shows microstructure after solidification. All structures seen in the image has close chemical composition to laves phases. Even the phase located on grain boundary shows a chemical composition similar to other structure in the image. No NbC or any other type of carbide located. Laves phases in Figure 4.19 had more blocky morphology seen from sand mould castings in Figure 4.11.

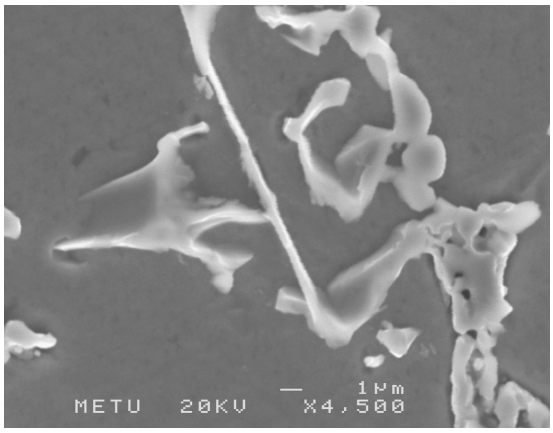

Figure 4.20. Script shape laves phase in the as-cast condition of metal casting.

Figure 4.20 shows another laves phase group formed in a "script-like" shape rather than a block one, as shown in Figure 4.19. The morphology was highly distorted compared to the compact eutectic-like shape of the laves phase from sand-casting, as seen in Figure 4.11. The chemical compositions of both morphologies in Figure 4.19 and Figure 4.20 taken by EDS are listed in Table 4.10.

Table 4.10. Chemical content of As-cast microstructure from metal mould castings.

Elements	Al	Si	Ti	Cr	Fe	Co	Ni	Nb	Mo
Blocky Laves	0.40	2.30	1.16	14.57	5.82	8.97	36.99	29.78	-
Script-like Laves	0.50	-	4.27	12.03	4.96	4.34	26.48	47.42	-
As-Cast (Matrix)	1.35	0.57	0.56	21.54	10.34	9.75	50.94	2.74	2.20

EDS analysis shows variation in composition. Script shape laves phase has higher Nb content. Meanwhile, EDS analysis shows a 2.30% Si for blocky laves, but not

for script laves. According to matrix chemical composition, Si is highly segregated towards granular laves phases.

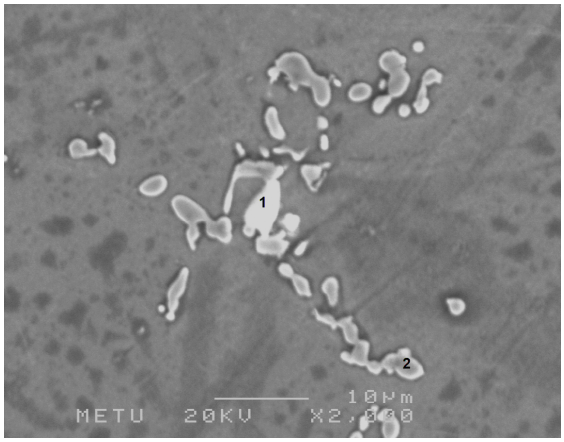

Figure 4.21. Metal mould casting in homogenized condition. Kalling 2 etchant used.

Figure 4.21 shows casting after homogenization. The structure chemical analysis is given below. Even after homogenization, laves-like structures were observed, as seen in Table 4.11. Random EDS analysis shows no structure different than the EDS results of Area Two in Figure 4.21. Except for area one, that seems to be either an Al_2O_3 particle remaining from polishing with an Al_2O_3 solution or a large inclusion from the melting process.

Table 4.11. Chemical content of homogenized microstructure from metal mould castings.

Elements	Al	Si	Ti	Cr	Fe	Co	Ni	Nb	Mo
Area 1	62.98	-	0.86	8.32	3.42	2.82	15.95	4.69	0.97
Area 2	0.25	2.62	3.21	14.33	5.87	9.26	31.74	42.72	-
Homogenized (Matrix)	1.29	0.53	0.82	20.63	9.59	9.35	50.23	4.96	2.59
As-Cast (Matrix)	1.35	0.57	0.56	21.54	10.34	9.75	50.94	2.74	2.20

After homogenization, a noticeable increase in certain elements, such as Ti, Nb, and Mo, is observed in the matrix, along with an apparent reduction in Cr, Fe, and Co. This indicates that homogenization has occurred to some extent. Laves at Area 2 has

more silicon content 2.62% than the laves phase in as-cast condition with 2.30% Si content

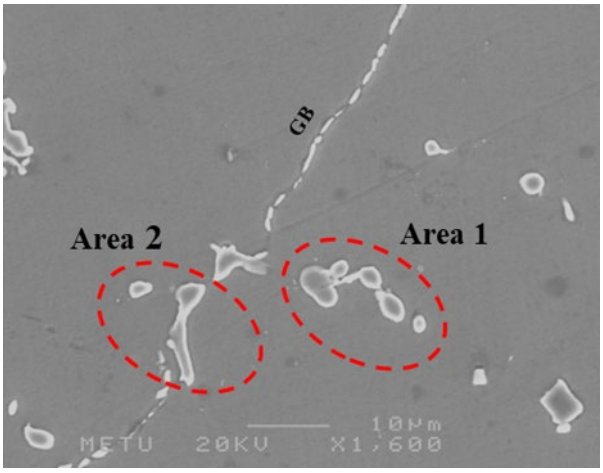

Figure 4.22. Metal casting in aged condition. Kalling 2 etchant used.

The aged condition is as in Figure 4.22. Similar granular structures remain after aging. Along the grain boundary, a phase formed in a film-like manner, a behavior typically associated with $Cr_{23}C_6$ in Alloy 718 or similar Ni-based superalloys.

The chemical content of the phases is listed in Table 4.12. EDS analysis identified granular-shaped phase laves phases, similar to those observed in both the as-cast and homogenized conditions. EDS analysis of the film-like structure along the grain boundary indicates a similar chemical composition. However, the Nb content is significantly lower, while the nickel and chromium contents are notably higher. This chemical variation may be attributed to instrumentation limitations, as the grain boundary structure is extremely thin, and the larger EDS spot size likely mixes signals from the surrounding matrix phase. Si content of laves phases in the aged condition was higher than other as-cast and homogenized conditions with its' 3.06 and 3.16% Si content. This result shows that Si is a significant element promoting laves phase and possibly indicates that laves phase during aging may dissolve or transform into something else. There is a correlation between grain boundary laves phase formation and reduction of laves phase in the matrix. In order to understand

the mechanism taken here, a Transmission Electron Microscope (TEM) is required for further analysis.

Table 4.12. Chemical content of aged microstructure from metal mould castings.

Elements	Al	Si	Ti	Cr	Fe	Co	Ni	Nb
Area 1	-	3.06	0.50	15.55	7.24	11.05	33.94	28.66
Area 2	-	3.16	0.86	15.13	6.39	11.67	32.74	30.07
Grain Boundary	0.65	2.08	0.68	18.92	8.64	10.56	43.06	15.41

The average laves phase composition was estimated using the JMatPro V7 solidification module and listed in Table 4.13. In the calculation. The solidification cut-off is set to 0.02% liquid. Although slight variations exist, Cr, Fe, Ni, and Nb exhibit similar ratios compared to Table 4.12 and Table 4.13 analysis. Si, Mo, and Co showed significant differences with the actual analysis. Mo diffraction peak is very close to Nb. Therefore, EDS could not differentiate these elements. The high amount of Nb covers Mo, resulting in no detection.

Table 4.13. JMatPro v7 estimation of laves phase composition.

Elements	Ni	Co	Cr	Fe	Mn	Mo	Nb	Si	Ti	W
Wt %	31.92	5.20	13.99	6.39	0.08	5.51	34.70	0.64	1.06	0.51

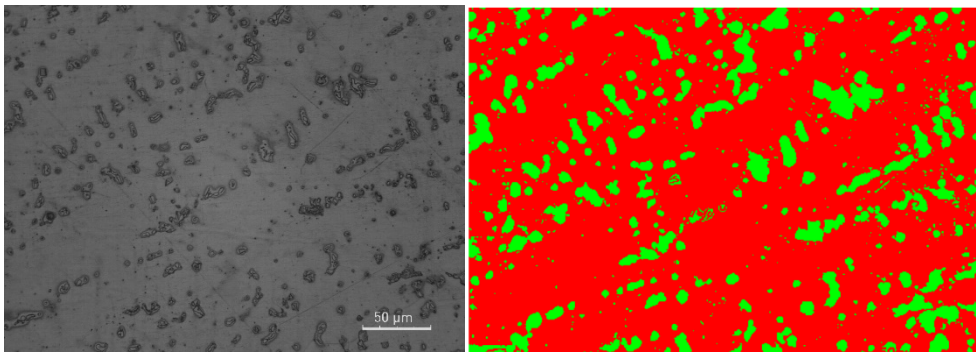

Figure 4.23. Metal mould casting under homogenized condition. Near Wall (Left-side) images captured at X1160 magnification with optical microscope. Kalling 2 etchant used.

Figure 4.23 is the microstructure near the metal mould surface. Due to etchants, the phase surrounding was over-etched. By increasing the contrast between phases and matrix, Figure 4.23b is created. Then, the coverage ratio of the colored areas was calculated. The analysis indicates that the red region occupies 83.25% of the total area, while the green region accounts for 16.75%.

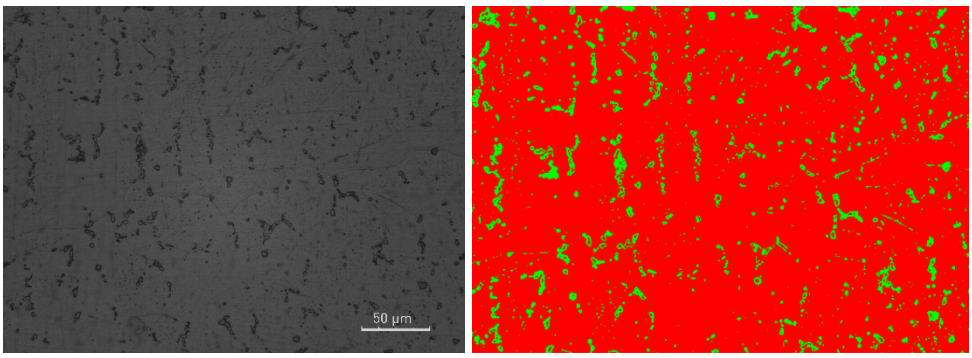

Figure 4.24. Metal mould casting, Homogenized condition. images captured from center with X1160 magnification. Kalling 2 etchant used.

Figure 4.24 presents the microstructure observed at the central region of the slab's cross-section. Visually, secondary structures look less and smaller compared with Figure 4.23. Similarly, a binary image was generated, and the area ratios were analyzed based on the color differences. The analysis revealed the following area distribution: red regions account for 92.74% of the total area, while green regions constitute 7.26%.

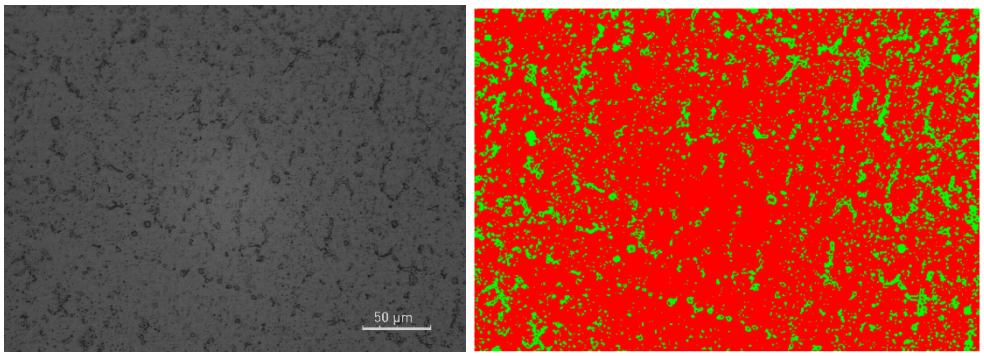

Figure 4.25. Metal mould casting, Homogenized condition. Near Wall (Right-side) images with X1160 magnification. Kalling 2 etchants used.

Figure 4.25 shows the other end of the cross-section. The secondary phases occupy a larger area than the central micrograph shown in Figure 4.24. However, their size is smaller than those observed at the left end of the specimen, highlighting a distinct difference. The analysis indicates that red regions account for 85.10% of the total area, while green regions constitute 14.90%.

Table 4.14. Quantitative results to evaluate the effectiveness of homogenization.

Location	Matrix Phase	Secondary Phases
Left End	83.25%	16.75%
Center	92.74%	7.26%
Right End	85.10%	14.90%

The goal of generating binary images was to identify distinct structures within the matrix rather than to differentiate them from one another. SEM analysis showed that Laves phase, TiN, and pores and inclusions like Al_2O_3 formed these structures. Since the formation of Laves phases is highly dependent on segregation during solidification, binary segmentation can assist in identifying the impact of cross-section thickness on the slab.

As seen from Table 4.14, the central areas were less populated than the sides, highlighting the significance of thickness on the solidification process. Consequently, the alloy's homogeneity is influenced by thickness, and the solidification conditions also determine the extent of phase dissolution during homogenization.

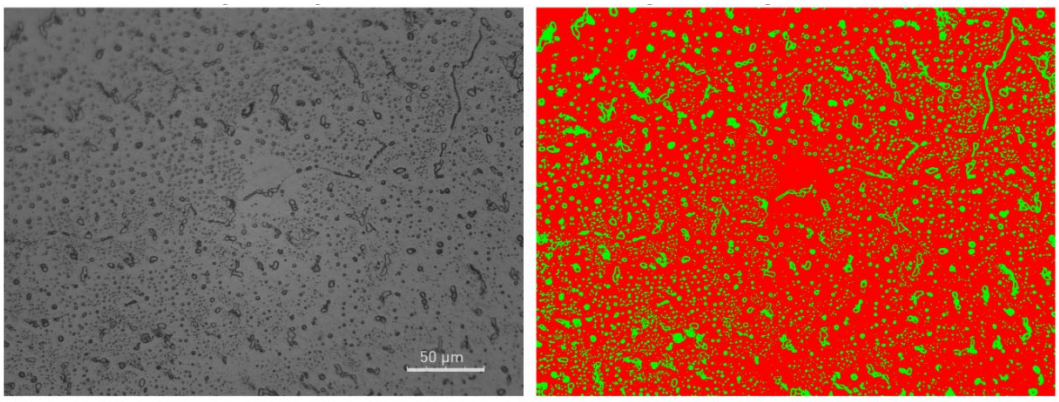

Figure 4.26. Metal mould casting in solution treated condition under optical microscope. x1160 magnification.

Micrograph in Figure 4.26 shows solution treated condition of castings with metal mould. The analysis indicates that the larger, bright phase is represented in red, occupying approximately 82.68% of the total area. In contrast, the smaller, dark phase, depicted in green, accounts for around 17.32% of the area.

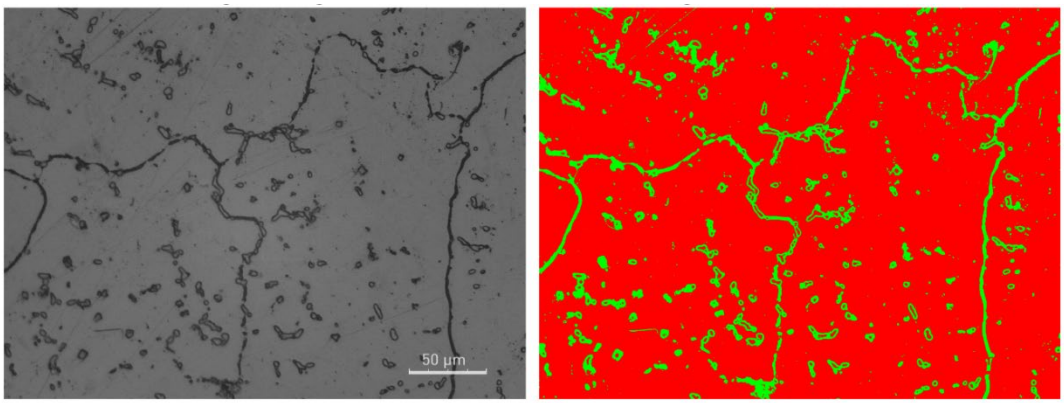

Figure 4.27. Metal mould casting in aged condition under optical microscope. x1160 magnification.

Figure 4.27 shows the alloys aged condition micrographs. The analysis reveals that the red region (Matrix phase) occupies approximately 91.39% of the total area. Conversely, the secondary phases, shown in green, account for about 8.61% of the area. Laves phase alongside the grain boundary was easily observable and aligned with SEM analysis's observations in Figure 4.22.

Table 4.15. Phase quantitative analysis for each heat treatment condition.

Condition	Matrix	Secondary phases
Homogenized	92.74%	7.26%
Solution Treated	82.68%	17.32%
Aged	91.39%	8.61%

The image analysis results in Figure 4.24, Figure 4.26, and Figure 4.27 are listed in Table 4.15. For comparability, all images were obtained from the central region of the specimens. It appears that certain phases began to precipitate within the matrix during the solution treatment. Following the aging treatment, the matrix phase appears brighter than its condition after the solution treatment. Meanwhile, a film-like phase formed nearly all the grain boundaries identified as laves phase in Figure 4.22. Following the solution treatment, granular and film-like phases formed along the grain boundaries, suggesting precipitation within the grain boundaries may have been initiated during the solution treatment process.

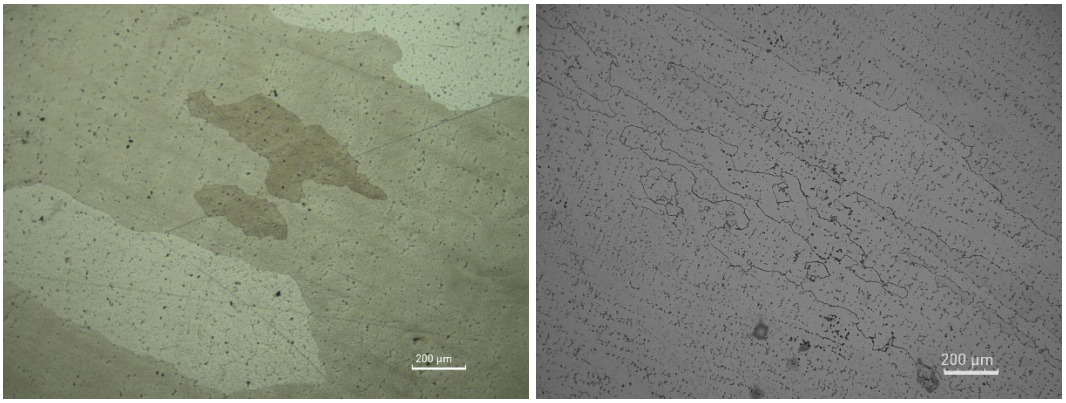

Figure 4.28. Sand casting and Metal mould casting under an optical microscope with x200 magnification.

In both castings, equiaxed grains were not achieved. Both castings have elongated columnar macro-grains. However, metal mould casting shows more irregular grain than sand casting, as seen in Figure 4.28. Individually, the number of grains observed

in a single micrograph is higher in metal mould casting. Therefore, sand casting produced larger grains.

Even after homogenization, the Laves phase remained present in the microstructure of the metal mould casting, with no NbC observed. In contrast, the sand casting showed no Laves phase but exhibited the presence of NbC after homogenization. This behavior can be attributed to differences in carbon addition, as the revert Alloy 718 used in the second casting contains a certain amount of carbon in its chemical composition. In contrast, no carbon was added during the third casting to minimize carbide formation in the structure.

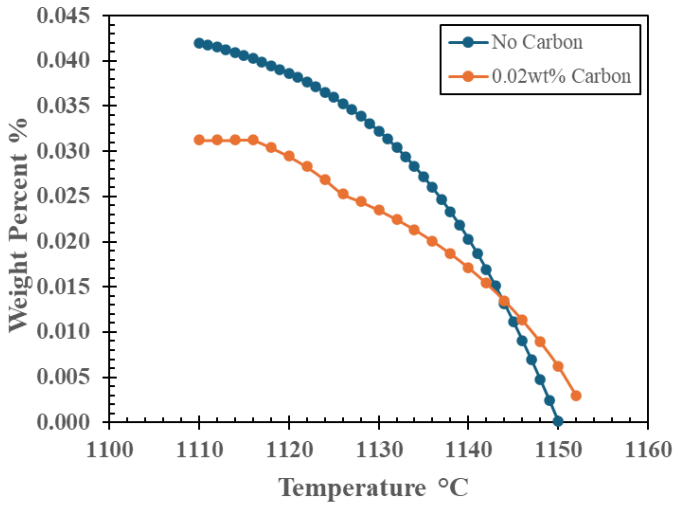

Figure 4.29. Estimated carbon influence over 718Plus solidification by JmatPro.

Figure 4.29 presents the influence of carbon on the laves phase in the solidification microstructure. A comparison is made between no carbon addition and the addition of 0.02% carbon, with all other elements remaining unchanged. The solidification cut-off is set at 0.02% percent liquid for each analysis. As the carbon content increases, the amount of laves phase decreases. This can be attributed to niobium being utilized by carbon to form carbides. In the absence of carbon in the composition, the laves phase is promoted. Unlike Alloy 718, 718Plus may require a minimum carbon limit to control laves phase amount, which is highly important for

homogenization effectiveness. However, max carbon content can lead to an overformation of NbC, resulting in the precipitation of film-like $M_{23}C_6$ during aging.

The analysis in Figure 4.29 suggests that the laves eutectic reaction point does not shift significantly enough to impact the effectiveness of the homogenization process. Additionally, the combined influence of carbon (C), silicon (Si), and the solidification rate may contribute to the behavior of the laves phase. One of the studies showed that cobalt addition to alloy 718 without any other composition modification when Ni kept a balance element[75]. The results showed an increase in Laves phase formation during solidification. Since the laves phase turned into an equilibrium phase with cobalt addition, laves phase were observed along the grain boundary after solution treatment[75]. As silicon content increases in the laves phase after each heat treatment step, this behavior may indicate that a lack of carbon and high Si content may turn laves into an equilibrium phase and make it difficult to dissolve completely.

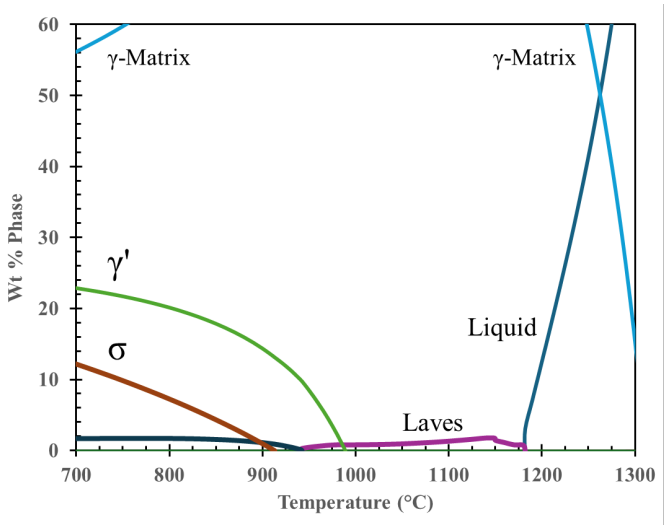

Figure 4.30. Equilibrium phase distribution diagram by JMatPro in different temperatures with 1% Si and 0% Carbon content.

High Si content (1%) with no carbon addition changed the phase distribution diagram as in Figure 4.30. Laves phase became equilibrium at temperatures 941 - 1182°C. Without getting temperatures above 1181°C, the dissolution of laves phase is

impossible. The maximum amount of laves phase should be observed at 1141 °C with 1.79 wt%. Laves phase can still exist in equilibrium at a solution treatment temperature of 968 °C but in low amounts. Below 941 °C, Laves phase cannot remain in the microstructure in an equilibrium state. Therefore, laves phase is not in an equilibrium state during aging; it is possible that the Laves phase partially dissolved and subsequently reformed along the grain boundary, as in Figure 4.27. From a kinetic point of view, the aging temperatures are too low for fast Nb diffusion, and even at high temperatures, homogenization is slow because of Nb.

CHAPTER 5

CONCLUSION AND FUTURE WORK

The literature shows extensive research aimed at replacing rotating forged Alloy 718 components with Alloy 718Plus, a chemically modified variant of Alloy 718. Similarly, significant efforts have focused on increasing engine operating temperatures. However, further advancements necessitate research into static components, an area that remains unpopular. Consequently, Alloy 718Plus has been selected as the focus of this thesis.

One casting was carried out using a sand mould, while the other was performed using a metal mould.

In sand castings, revert alloy 718 is used for alloying. Mechanical tests show that the alloy retains its ductility after 8 hours of homogenization. Metallographic evaluation indicates no Laves phase is observed after homogenization. However, a high amount of NbC remains, even with the addition of 2% excess cobalt.

It has been demonstrated that by adding alloying elements, Alloy 718 can be utilized as revert and transformed into 718Plus, presenting a significant opportunity for recycling and reusing the alloy in future applications.

In the metal mould, alloying was carried out entirely using elemental raw materials. XRF analysis confirmed that the primary alloying elements were at the correct levels. No additional carbon was introduced to minimize NbC formation. The metallographic evaluation showed no NbC formation but promoted Laves formation, exhibiting morphological differences compared to those in the sand cast. Additionally, the quantity of Laves phases was excessive, and homogenization had minimal effect, even with increased holding temperature and time. Due to this difference, the alloy was difficult to machine. Following solution treatment and aging, Laves phases formed along grain boundaries in a film-like structure.

Future work will focus on refining the casting process and understanding the microstructural behavior of 718Plus. Several action that will be important listed below within the scope of this thesis.

1. SDAS and grain size control by manipulating thickness, pouring temperature and mould temperature in investment casting.
2. Effect of different carbon and silicon levels to laves formation and homogenization effectiveness
3. NbC amount, size, and the effect of NbC dissolution
4. Mechanism of laves phase dissolution in aging when laves phase can remain in equillibrium state.

REFERENCES

[1] Kennedy, R. L., 2005, "Allvac 718Plus, Superalloy for the Next Forty Years," *Superalloys 718, 625, 706 and Various Derivatives (2005)*, TMS, pp. 1–14. https://doi.org/10.7449/2005/Superalloys_2005_1_14.

[2] Lippold, J. C., 2009, *Welding Metallurgy and Weldability of Nickel-Base Alloys*, Wiley, Hoboken.

[3] Schafrik, R. E., Ward, D. D., and Groh, J. R., 2001, "Application of Alloy 718 in GE Aircraft Engines: Past, Present and Next Five Years," *Superalloys 718, 625, 706 and Various Derivatives (2001)*, TMS, pp. 1–11. https://doi.org/10.7449/2001/Superalloys_2001_1_11.

[4] Ott, E. A., Groh, J., and Sizek, H., 2005, "Metals Affordability Initiative: Application of Allvac Alloy 718Plus for Aircraft Engine Static Structural Components," *Superalloys 718, 625, 706 and Various Derivatives (2005)*, TMS, pp. 35–45. https://doi.org/10.7449/2005/Superalloys_2005_35_45.

[5] Rolls-Royce Limited and Rolls-Royce Plc, eds., 2005, *The Jet Engine*, Rolls-Royce plc, London.

[6] McCreath, C. G., 1987, "Hot Corrosion Site Environment in Gas Turbines," Materials Science and Technology, **3**(7), pp. 494–500. https://doi.org/10.1080/02670836.1987.11782260.

[7] Goward, G. W., 1986, "Low-Temperature Hot Corrosion in Gas Turbines: A Review of Causes and Coatings Therefor," Journal of Engineering for Gas Turbines and Power, **108**(2), pp. 421–425. https://doi.org/10.1115/1.3239921.

[8] Garibov, G. S., Grits, N. M., Vostrikov, A. V., Fedorenko, Y. A., and Volkov, A. M., 2014, "Development of Advanced P/M Ni-Base Superalloys for Turbine Disks," MATEC Web of Conferences, **14**, p. 17001. https://doi.org/10.1051/matecconf/20141417001.

[9] Koizumi, Y., Kobayashi, T., Yokokawa, T., Zhang, J., Osawa, M., Harada, H., Aoki, Y., and Arai, M., 2004, "Development of Next-Generation Ni-Base Single Crystal Superalloys," *Superalloys 2004 (Tenth International Symposium)*, TMS, pp. 35–43. https://doi.org/10.7449/2004/Superalloys_2004_35_43.

[10] Bakradze, M. M., Ovsepyan, S. V., Buiakina, A. A., and Lomberg, B. S., 2018, "Development of Ni-Base Superalloy with Operating Temperature up to 800°C for Gas Turbine Disks," Inorg. Mater. Appl. Res., **9**(6), pp. 1044–1050. https://doi.org/10.1134/S2075113318060035.

[11] Kawagishi, K., Yeh, A., Yokokawa, T., Kobayashi, T., Koizumi, Y., and Harada, H., "Development of an Oxidation-Resistant High-Strength Sixth-Generation Single-Crystal Superalloy TMS-238."

[12] Wu K., Liua G., Hu B., Ma W., Zhang Y., Tao Y., and Liu J., 2012, "Forging process of a new type high-performance P/M turbine disk superalloy," Procedia Engineering, **27**, pp. 954–968. https://doi.org/10.1016/j.proeng.2011.12.542.

[13] Sato, A., Harada, H., Yokokawa, T., Murakumo, T., Koizumi, Y., Kobayashi, T., and Imai, H., 2006, "The Effects of Ruthenium on the Phase Stability of Fourth Generation Ni-Base Single Crystal Superalloys," Scripta Materialia, **54**(9), pp. 1679–1684. https://doi.org/10.1016/j.scriptamat.2006.01.003.

[14] Gabb, T. P., MacKay, R. A., Draper, S. L., Sudbrack, C. K., and Nathal, M. V., 2013, "The Mechanical Properties of Candidate Superalloys for a Hybrid Turbine Disk."

[15] Fecht, H., and Furrer, D., 2000, "Processing of Nickel-Base Superalloys for Turbine Engine Disc Applications," Adv. Eng. Mater., **2**(12), pp. 777–787. https://doi.org/10.1002/1527-2648(200012)2:12<777::AID-ADEM777>3.0.CO;2-R.

[16] Smallman, R. E., and Ngan, A. H. W., 2014, *Modern Physical Metallurgy*, Elsevier/Butterworth-Heinemann, Oxford Waltham, MA.

[17] Donachie, M. J., and Donachie, S. J., 2002, *Superalloys: A Technical Guide*, ASM International, Materials Park, OH.

[18] Reed, R. C., 2006, *The Superalloys: Fundamentals and Applications*, Cambridge University Press, Cambridge, UK; New York. [Online]. Available: http://www.books24x7.com/marc.asp?bookid=35667. [Accessed: 01-Jul-2022].

[19] Jena, A. K., and Chaturvedi, M. C., 1984, "The Role of Alloying Elements in the Design of Nickel-Base Superalloys," J Mater Sci, **19**(10), pp. 3121–3139. https://doi.org/10.1007/BF00549796.

[20] Wu, Q., Li, S.-S., Ma, Y., and Gong, S.-K., 2012, "First Principles Calculations of Alloying Element Diffusion Coefficients in Ni Using the Five-Frequency Model," Chinese Phys. B, **21**(10), p. 109102. https://doi.org/10.1088/1674-1056/21/10/109102.

[21] Long, H., Mao, S., Liu, Y., Zhang, Z., and Han, X., 2018, "Microstructural and Compositional Design of Ni-Based Single Crystalline Superalloys — A Review," Journal of Alloys and Compounds, **743**, pp. 203–220. https://doi.org/10.1016/j.jallcom.2018.01.224.

[22] Wu, L., Osada, T., Watanabe, I., Yokokawa, T., Kobayashi, T., and Kawagishi, K., 2021, "Strength Prediction of Ni-Base Disc Superalloys: Modified Γ′ Hardening Models Applicable to Commercial Alloys," Materials Science and Engineering: A, **799**, p. 140103. https://doi.org/10.1016/j.msea.2020.140103.

[23] Sudakov, V. S., 1994, "Structure and Properties of a Large Forged Disk of KhN73MBTYu-VD (ÉI 698-VD)," Met Sci Heat Treat, **36**(2), pp. 94–98. https://doi.org/10.1007/BF01390295.

[24] Nembach, E., Schänzer, S., Schröer, W., and Trinckauf, K., 1988, "Hardening of Nickel-Base Superalloys by High Volume Fractions of γ'-Precipitates," Acta Metallurgica, **36**(6), pp. 1471–1479. https://doi.org/10.1016/0001-6160(88)90214-3.

[25] Reed, R. C., Tao, T., and Warnken, N., 2009, “Alloys-By-Design: Application to Nickel-Based Single Crystal Superalloys,” Acta Materialia, **57**(19), pp. 5898–5913. https://doi.org/10.1016/j.actamat.2009.08.018.

[26] Cozar, R., and Pineau, A., 1973, “Morphology of y’ and y” Precipitates and Thermal Stability of Inconel 718 Type Alloys,” MT, **4**(1), pp. 47–59. https://doi.org/10.1007/BF02649604.

[27] Oblak, J. M., Duvall, D. S., and Paulonis, D. F., 1974, “An Estimate of the Strengthening Arising from Coherent, Tetragonally-Distorted Particles,” Materials Science and Engineering, **13**(1), pp. 51–56. https://doi.org/10.1016/0025-5416(74)90020-2.

[28] Gabb, T. P., Backman, D. G., Wei, D. Y., Mourer, D. P., Furrer, D., Garg, A., and Ellis, D. L., “Y’ FORMATION IN A NICKEL-BASE DISK SUPERALLOY.”

[29] Semiatin, S. L., Mahaffey, D. W., Levkulich, N. C., Senkov, O. N., and Tiley, J. S., 2018, “The Effect of Cooling Rate on High-Temperature Precipitation in a Powder-Metallurgy, Gamma/Gamma-Prime Nickel-Base Superalloy,” Metall Mater Trans A, **49**(12), pp. 6265–6276. https://doi.org/10.1007/s11661-018-4896-5.

[30] Han, Y., Deb, P., and Chaturvedi, M. C., 1982, “Coarsening Behaviour of Γ″- and Γ′-Particles in Inconel Alloy 718,” Metal Science, **16**(12), pp. 555–562. https://doi.org/10.1179/030634582790427118.

[31] Sundararaman, M., and Mukhopadhyay, P., 1993, “Carbide Precipitation in Inconel 718,” High Temperature Materials and Processes, **11**(1–4), pp. 351–368. https://doi.org/10.1515/HTMP.1993.11.1-4.351.

[32] Formenti, A., Eliasson, A., Mitchell, A., and Fredriksson, H., 2005, “Solidification Sequence and Carbide Precipitation in Ni-Base Superalloys In718, In625 and In939,” High Temperature Materials and Processes, **24**(4), pp. 239–258. https://doi.org/10.1515/HTMP.2005.24.4.239.

[33] Knorovsky, G. A., Cieslak, M. J., Headley, T. J., Romig, A. D., and Hammetter, W. F., 1989, "INCONEL 718: A Solidification Diagram," Metall Trans A, **20**(10), pp. 2149–2158. https://doi.org/10.1007/BF02650300.

[34] Ferreri, N. C., Vogel, S. C., and Knezevic, M., 2020, "Determining Volume Fractions of γ, Γ′, Γ″, δ, and MC-Carbide Phases in Inconel 718 as a Function of Its Processing History Using an Advanced Neutron Diffraction Procedure," Materials Science and Engineering: A, **781**, p. 139228. https://doi.org/10.1016/j.msea.2020.139228.

[35] Collins, H. E., 1968, "Relative Stability of Carbide and Intermetallic Phases in Nickel-Base Superalloys," *International Symposium on Structural Stability in Superalloys (1968)*, TMS, pp. 171–198. https://doi.org/10.7449/1968/Superalloys_1968_171_198.

[36] Rae, C. M. F., and Reed, R. C., 2001, "The Precipitation of Topologically Close-Packed Phases in Rhenium-Containing Superalloys," Acta Materialia, **49**(19), pp. 4113–4125. https://doi.org/10.1016/S1359-6454(01)00265-8.

[37] Belan, J., 2016, "GCP and TCP Phases Presented in Nickel-Base Superalloys," Materials Today: Proceedings, **3**(4), pp. 936–941. https://doi.org/10.1016/j.matpr.2016.03.024.

[38] Wilson, A. S., 2017, "Formation and Effect of Topologically Close-Packed Phases in Nickel-Base Superalloys," Materials Science and Technology, **33**(9), pp. 1108–1118. https://doi.org/10.1080/02670836.2016.1187335.

[39] Biss, V., Kirby, G. N., and Sponseller, D. L., "The Relative Effects of Chromium, Molybdenum, Tungsten, and Tantalum on the Occurrence of Phase in Cast Ni-Co-Cr Alloys," METALLURGICAL TRANSACTIONS A.

[40] Stein, F., and Leineweber, A., 2021, "Laves Phases: A Review of Their Functional and Structural Applications and an Improved Fundamental Understanding of Stability and Properties," J Mater Sci, **56**(9), pp. 5321–5427. https://doi.org/10.1007/s10853-020-05509-2.

[41] Cieslak, M. J., Knorovsky, G. A., Headley, T. J., and Romig, Jr, A. D., 1989, "The Solidification Metallurgy of Alloy 718 and Other Nb-Containing Superalloys," *Superalloys 718 Metallurgy and Applications (1989)*, TMS, pp. 59–68. https://doi.org/10.7449/1989/Superalloys_1989_59_68.

[42] Murata, Y., Morinaga, M., Yukawa, N., Ogawa, H., and Kato, M., 1994, "Solidification Structures of Inconel 718 with Microalloying Elements," *Superalloys 718, 625, 706 and Various Derivatives (1994)*, TMS, pp. 81–88. https://doi.org/10.7449/1994/Superalloys_1994_81_88.

[43] Sohrabi, M. J., Mirzadeh, H., and Rafiei, M., 2018, "Solidification Behavior and Laves Phase Dissolution during Homogenization Heat Treatment of Inconel 718 Superalloy," Vacuum, **154**, pp. 235–243. https://doi.org/10.1016/j.vacuum.2018.05.019.

[44] Schirra, J. J., Caless, R. H., and Hatala, R. W., 1991, "The Effect of Laves Phase on the Mechanical Properties of Wrought and Cast + HIP Inconel 718," *Superalloys 718, 625 and Various Derivatives (1991)*, TMS, pp. 375–388. https://doi.org/10.7449/1991/Superalloys_1991_375_388.

[45] Oradei-Basile, A., and Radavich, J. F., 1991, "A Current T-T-T Diagram for Wrought Alloy 718," *Superalloys 718, 625 and Various Derivatives (1991)*, TMS, pp. 325–335. https://doi.org/10.7449/1991/Superalloys_1991_325_335.

[46] Azadian, S., Wei, L.-Y., and Warren, R., 2004, "Delta Phase Precipitation in Inconel 718," Materials Characterization, **53**(1), pp. 7–16. https://doi.org/10.1016/j.matchar.2004.07.004.

[47] Beaubois, V., Huez, J., Coste, S., Brucelle, O., and Lacaze, J., 2004, "Short Term Precipitation Kinetics of Delta Phase in Strain Free Inconel* 718 Alloy," Materials Science and Technology, **20**(8), pp. 1019–1026. https://doi.org/10.1179/026708304225019830.

[48] Cai, D., Zhang, W., Nie, P., Liu, W., and Yao, M., 2007, "Dissolution Kinetics of δ Phase and Its Influence on the Notch Sensitivity of Inconel 718," Materials

Characterization, **58**(3), pp. 220–225. https://doi.org/10.1016/j.matchar.2006.04.020.

[49] Desvallees, Y., Bouzidi, M., Bois, F., and Beaude, N., 1994, "Delta Phase in INCONEL 718: Mechanical Properties and Forging Process Requirements," *Superalloys 718, 625, 706 and Various Derivatives (1994)*, TMS, pp. 281–291. https://doi.org/10.7449/1994/Superalloys_1994_281_291.

[50] Zhang, H., Li, C., Guo, Q., Ma, Z., Huang, Y., Li, H., and Liu, Y., 2017, "Delta Precipitation in Wrought Inconel 718 Alloy; the Role of Dynamic Recrystallization," Materials Characterization, **133**, pp. 138–145. https://doi.org/10.1016/j.matchar.2017.09.032.

[51] Pickering, E. J., Mathur, H., Bhowmik, A., Messé, O. M. D. M., Barnard, J. S., Hardy, M. C., Krakow, R., Loehnert, K., Stone, H. J., and Rae, C. M. F., 2012, "Grain-Boundary Precipitation in Allvac 718Plus," Acta Materialia, **60**(6–7), pp. 2757–2769. https://doi.org/10.1016/j.actamat.2012.01.042.

[52] Cai, D., Zhang, W., Nie, P., Liu, W., and Yao, M., 2007, "Dissolution Kinetics of δ Phase and Its Influence on the Notch Sensitivity of Inconel 718," Materials Characterization, **58**(3), pp. 220–225. https://doi.org/10.1016/j.matchar.2006.04.020.

[53] Wang, M., Du, J., Deng, Q., Tian, Z., and Zhu, J., 2015, "The Effect of Phosphorus on the Microstructure and Mechanical Properties of ATI 718Plus Alloy," Materials Science and Engineering: A, **626**, pp. 382–389. https://doi.org/10.1016/j.msea.2014.12.094.

[54] Cao, W.-D., and Kennedy, R. L., 1994, "The Effect of Phosphorous on Mechanical Properties of Alloy 718," *Superalloys 718, 625, 706 and Various Derivatives (1994)*, TMS, pp. 463–477. https://doi.org/10.7449/1994/Superalloys_1994_463_477.

[55] Cao, W.-D., and Kennedy, R., 2004, "Role of Chemistry in 718-Type Alloys: Allvac 718plus Alloy Development," *Superalloys 2004 (Tenth International*

Symposium), TMS, pp. 91–99. https://doi.org/10.7449/2004/Superalloys_2004_91_99.

[56] Гюлиханданов, Е. Л., and Алексеева, Е. Л., “Влияние термической обработки на структуру и свойства сплава ЭП718.”

[57] Cao, W., 2008, “Thermal Stability Characterization of Ni-Base ATI 718Plus Superalloy,” *Superalloys 2008 (Eleventh International Symposium)*, TMS, pp. 789–797. https://doi.org/10.7449/2008/Superalloys_2008_789_797.

[58] AMS F Corrosion and Heat Resistant Alloys Committee, “Nickel Alloy, Corrosion- and Heat-Resistant, Bars, Forgings, and Rings Ni - 18Cr - 2.8Mo - 5.5Cb(Nb) - 0.70Ti - 1.50Al - 10Fe - 9Co - 1W Consumable Electrode Remelted or Vacuum Induction Melted 1775 °F (968 °C) Solution and Precipitation Heat Treated.” https://doi.org/10.4271/AMS5442B.

[59] Radis, R., Zickler, G. A., Stockinger, M., Sommitsch, C., and Kozeschnik, E., 2010, “Interaction of the Precipitation Kinetics of δ And γ’ Phases in Nickel-Base Superalloy ATI Allvac® 718Plus™,” MSF, **638–642**, pp. 2712–2717. https://doi.org/10.4028/www.scientific.net/MSF.638-642.2712.

[60] Tang, L., Zhang, H., Guo, Q., Liu, C., Li, C., and Liu, Y., 2021, “The Precipitation of η Phase during the Solution Treatments of Allvac 718Plus,” Materials Characterization, **176**, p. 111142. https://doi.org/10.1016/j.matchar.2021.111142.

[61] Cao, W.-D., 2005, “Solidification and Solid State Phase Transformation of Allvac 718Plus Alloy,” *Superalloys 718, 625, 706 and Various Derivatives (2005)*, TMS, pp. 165–177. https://doi.org/10.7449/2005/Superalloys_2005_165_177.

[62] Gaskell, D. R., and Laughlin, D. E., 2017, *Introduction to the Thermodynamics of Materials, Sixth Edition*, CRC Press. https://doi.org/10.1201/9781315119038.

[63] Sjöberg, G., 2012, "Casting Superalloys for Structural Applications," *Superalloy 718 and Derivatives*, E.A. Ott, J.R. Groh, A. Banik, I. Dempster, T.P. Gabb, R. Helmink, X. Liu, A. Mitchell, G.P. Sjöberg, and A. Wusatowska-Sarnek, eds., John Wiley & Sons, Inc., Hoboken, NJ, USA, pp. 116–130. https://doi.org/10.1002/9781118495223.ch8.

[64] Bayha, T. D., Lu, M., and Kloske, K. E., 2005, "Investment Casting of Allvac 718Plus Alloy," *Superalloys 718, 625, 706 and Various Derivatives (2005)*, TMS, pp. 223–232. https://doi.org/10.7449/2005/Superalloys_2005_223_232.

[65] Antonsson, T., and Fredriksson, H., 2005, "The Effect of Cooling Rate on the Solidification of INCONEL 718," Metall Mater Trans B, **36**(1), pp. 85–96. https://doi.org/10.1007/s11663-005-0009-0.

[66] Shi, X., Duan, S.-C., Yang, W.-S., Guo, H.-J., and Guo, J., 2018, "Effect of Cooling Rate on Microsegregation During Solidification of Superalloy INCONEL 718 Under Slow-Cooled Conditions," Metall Mater Trans B, **49**(4), pp. 1883–1897. https://doi.org/10.1007/s11663-018-1169-z.

[67] Kurz, W., Kurz, W., Fisher, D. J., and Fisher, D. J., 2005, *Fundamentals of Solidification*, Trans Tech Publ, Uetikon-Zuerich.

[68] Patel, A. D., and Murty, Y. V., 2001, "Effect of Cooling Rate on Microstructural Development in Alloy 718," *Superalloys 718, 625, 706 and Various Derivatives (2001)*, TMS, pp. 123–132. https://doi.org/10.7449/2001/Superalloys_2001_123_132.

[69] Andersson, J., Sjöberg, G., and Larsson, J., "Investigation of Homogenization and Its Influence on the Repair Welding of Cast Allvac 718Plus®," p. 16.

[70] Saunders, N., Guo, U. K. Z., Li, X., Miodownik, A. P., and Schillé, J.-Ph., 2003, "Using JMatPro to Model Materials Properties and Behavior," JOM, **55**(12), pp. 60–65. https://doi.org/10.1007/s11837-003-0013-2.

[71] AMS F Corrosion and Heat Resistant Alloys Committee, "Heat Treatment, Cast Nickel Alloy and Cobalt Alloy Parts." https://doi.org/10.4271/AMS2773F.

[72] AMS F Corrosion Heat Resistant Alloys Committee, “Heat Treatment Wrought Nickel Alloy and Cobalt Alloy Parts.” https://doi.org/10.4271/AMS2774.

[73] El-Bagoury, N., Matsuba, T., Yamamoto, K., Miyahara, H., and Ogi, K., 2005, “Influence of Heat Treatment on the Distribution of Ni2Nb and Microsegregation in Cast Inconel 718 Alloy,” Mater. Trans., **46**(11), pp. 2478–2483. https://doi.org/10.2320/matertrans.46.2478.

[74] Cockcroft, S. L., Degawa, T., Mitchell, A., Tripp, D. W., and Schmalz, A., 1992, “Inclusion Precipitation in Superalloys,” *Superalloys 1992 (Seventh International Symposium)*, TMS, pp. 577–586. https://doi.org/10.7449/1992/Superalloys_1992_577_586.

[75] Yao, X., Liu, F., Yang, S., Liu, D., Jia, D., and Sun, W., 2021, “Effect of Cobalt on the Precipitation of Laves, Γ′ and Γ″ Phases in a 718 Base Alloy with 1.2 Wt.% Al,” Journal of Materials Research and Technology, **15**, pp. 4427–4436. https://doi.org/10.1016/j.jmrt.2021.10.068.

APPENDICES

A. EDS Analysis

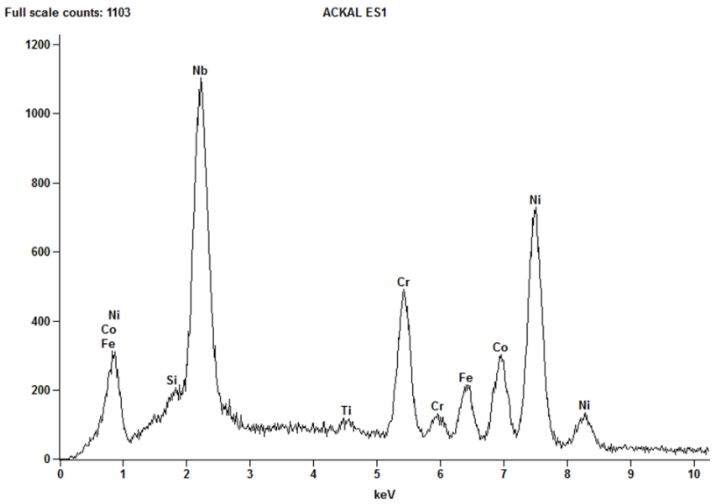

Fig A. 1. EDS Analysis of laves phase in sand casting.

Fig A. 1 shows laves phase EDS analysis from Table 4.7.

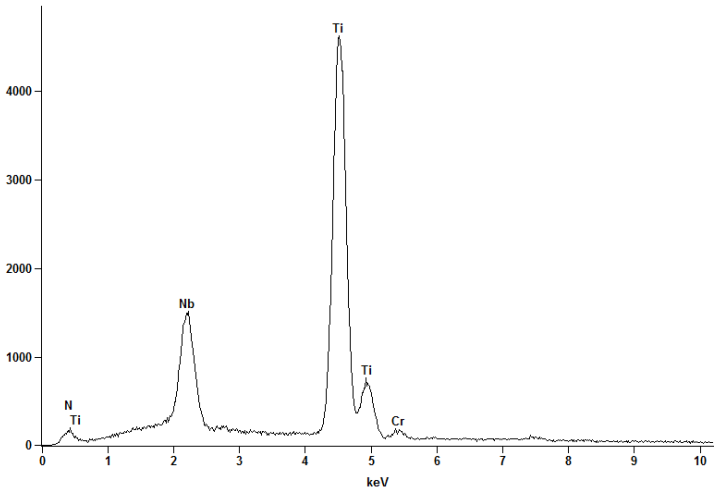

Fig A. 2. EDS analysis of Phase A.

X-ray peaks from EDS analysis of Phase A from Table 4.8.

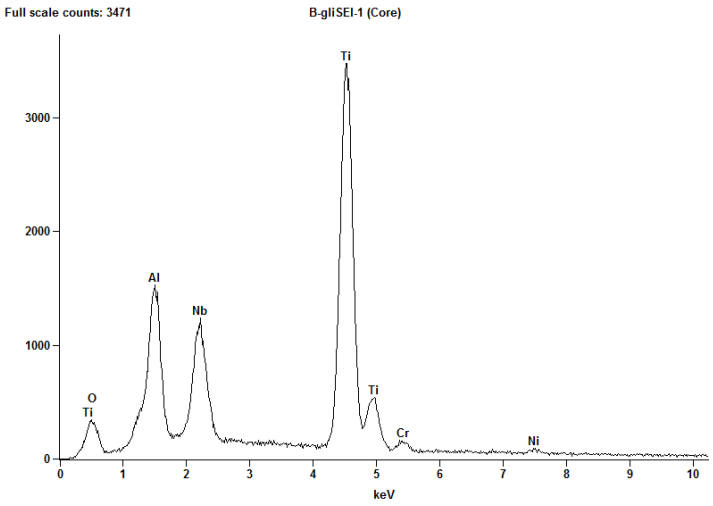

Fig A. 3. EDS analysis of Phase B.

X-Ray peaks from EDS taken from Table 4.8 Phase B.

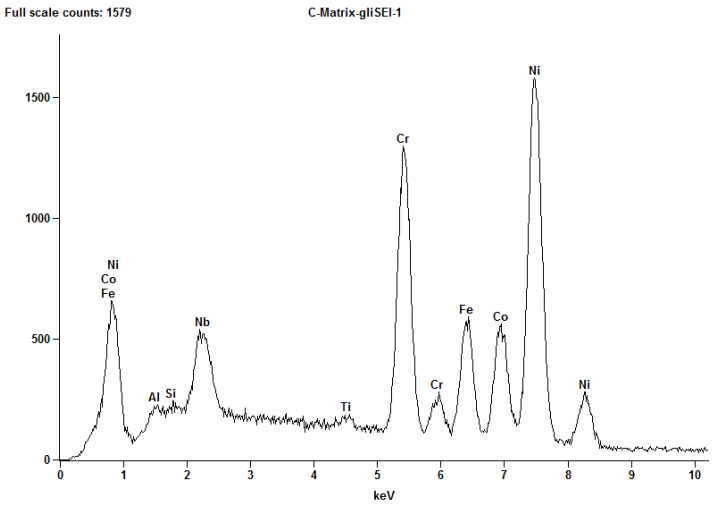

Fig A. 4. EDS analysis of Phase c.

X-Ray peaks from EDS taken from Table 4.8 Phase C.

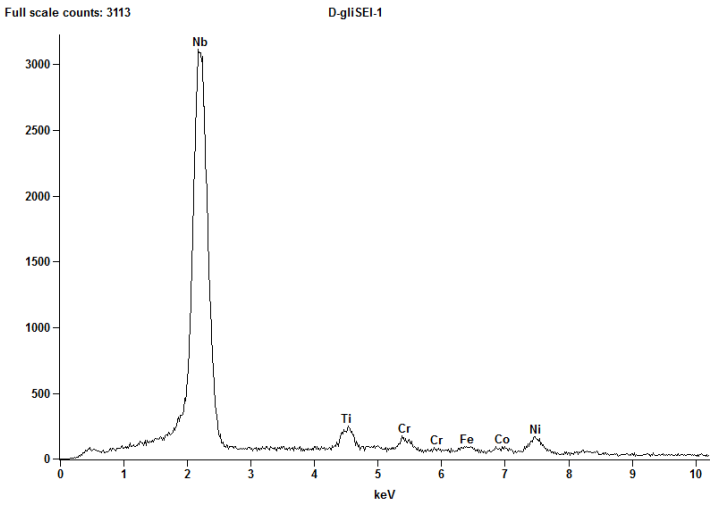

Fig A. 5. EDS analysis of Phase D

X-Ray peaks from EDS taken from Table 4.8 Phase D.

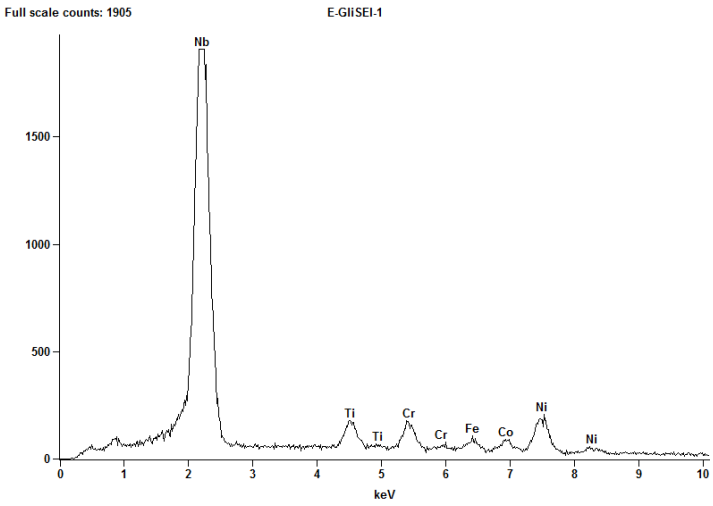

Fig A. 6. EDS analysis of Phase E

X-Ray peaks from EDS taken from Table 4.8 Phase E.